Article

Cell Systems

Environment Tunes Propagation of Cell-to-Cell Variation in the Human Macrophage Gene Network

Graphical Abstract

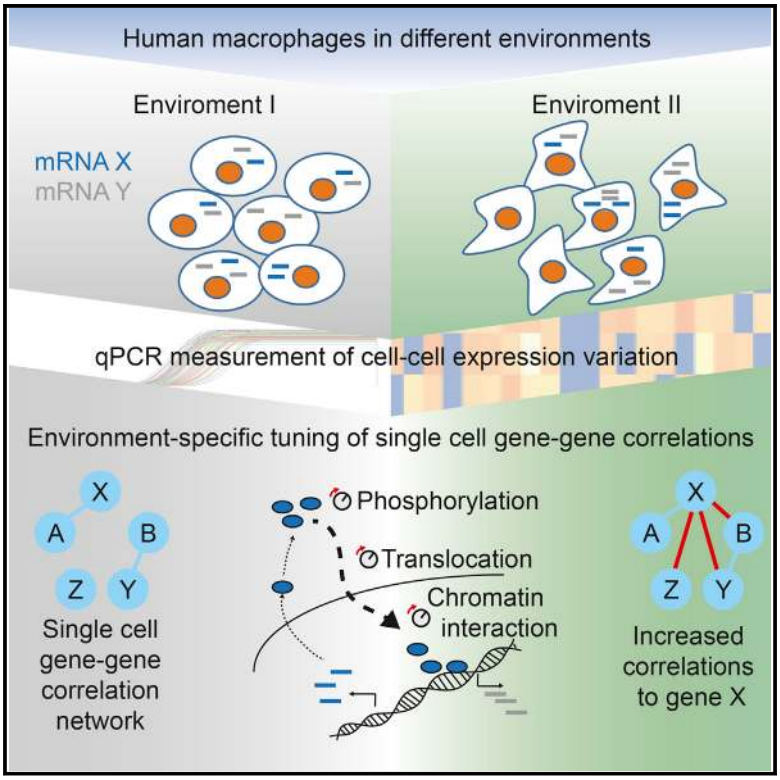

Authors

Andrew J. Martins, Manikandan Narayanan, Thorsten Prüstel, ..., William W. Lau, Katherine V. Wendelsdorf, John S. Tsang

Correspondence

john.tsang@nih.gov

In Brief

Martins and Narayanan et al. use single-cell analysis of human macrophages exposed to distinct cytokines combined with flow cytometry, imaging, epigenomic, and in silico stochastic simulation analyses to reveal how cell-to-cell expression variation in one gene can propagate to other genes in an environment-dependent manner to potentially shape cellular heterogeneity.

Highlights

- Propagation of variation (PoV) in gene expression depends on biochemical parameters
- Different cytokine environments can tune system parameters to affect PoV
- Transcription factor activity and interaction with target enhancers can tune PoV
- Natural perturbation of cellular and biochemical parameters can reveal PoV regulators

Martins et al., 2017, Cell Systems *4*, 379–392
April 26, 2017
http://dx.doi.org/10.1016/j.cels.2017.03.002

CellPress

Cell Systems
Article

Environment Tunes Propagation of Cell-to-Cell Variation in the Human Macrophage Gene Network

Andrew J. Martins,[1,7] Manikandan Narayanan,[1,7] Thorsten Prüstel,[2] Bethany Fixsen,[1] Kyemyung Park,[1,3] Rachel A. Gottschalk,[4] Yong Lu,[1] Cynthia Andrews-Pfannkoch,[1,8] William W. Lau,[5] Katherine V. Wendelsdorf,[1,9] and John S. Tsang[1,6,10,*]

[1]Systems Genomics and Bioinformatics Unit
[2]Computational Biology Section
Laboratory of Systems Biology, National Institutes of Health, Bethesda, MD 20892, USA
[3]Biophysics Program, University of Maryland-NIH Graduate Partnership Program, University of Maryland, College Park, MD 20742, USA
[4]Lymphocyte Biology Section, Laboratory of Systems Biology
[5]Office of Intramural Research, Center for Information Technology
[6]Trans-NIH Center for Human Immunology (CHI)
National Institutes of Health, Bethesda, MD 20892, USA
[7]Co-first author
[8]Present address: Department of Ophthalmology, Mayo Clinic, Rochester, MN 55905, USA
[9]Present address: Qiagen, Inc., Redwood City, CA 94063, USA
[10]Lead Contact
*Correspondence: john.tsang@nih.gov
http://dx.doi.org/10.1016/j.cels.2017.03.002

SUMMARY

Cell-to-cell variation in gene expression and the propagation of such variation (PoV or "noise propagation") from one gene to another in the gene network, as reflected by gene-gene correlation across single cells, are commonly observed in single-cell transcriptomic studies and can shape the phenotypic diversity of cell populations. While gene network "rewiring" is known to accompany cellular adaptation to different environments, how PoV changes between environments and its underlying regulatory mechanisms are less understood. Here, we systematically explored context-dependent PoV among genes in human macrophages, utilizing different cytokines as natural perturbations of multiple molecular parameters that may influence PoV. Our single-cell, epigenomic, computational, and stochastic simulation analyses reveal that environmental adaptation can tune PoV to potentially shape cellular heterogeneity by changing parameters such as the degree of phosphorylation and transcription factor-chromatin interactions. This quantitative tuning of PoV may be a widespread, yet underexplored, property of cellular adaptation to distinct environments.

INTRODUCTION

Single-cell expression data have revealed pervasive cell-to-cell variability in mRNA and protein expression, even within isogenic cell populations exposed to identical environments (Altschuler and Wu, 2010; Eldar and Elowitz, 2010; Raj and van Oudenaarden, 2008). Such cell-to-cell differences in gene expression can arise due to a combination of "intrinsic" (e.g., inherent stochasticity in biochemical reactions underlying gene and protein expression) and "extrinsic" (e.g., differences in the micro-environment or ribosome concentration of individual cells) factors. Importantly, variability in the expression of one gene can be propagated to other genes in the underlying network (Pedraza and van Oudenaarden, 2005; Rosenfeld et al., 2005); for example, cells expressing higher levels of a transcription factor (TF) could express higher levels of target genes activated by the TF. Propagation of expression variability could contribute to phenotypic differences among cells, such as the cell-to-cell variability previously described for cellular differentiation potential (Chang et al., 2008), adaptation to environmental fluctuations (Kussell and Leibler, 2005), or responsiveness upon cellular activation (Feinerman et al., 2008). Such diversification of cellular phenotypes can serve important functions at the cell population level, such as generating functionally distinct cell subsets and ensuring that a fraction of cells function properly despite unpredictable environmental changes (Acar et al., 2008; Kussell and Leibler, 2005; Thattai and van Oudenaarden, 2004).

The propagation of variation (PoV; sometimes referred to as "noise propagation") of gene expression in regulatory networks has been studied using a number of approaches, including experimentally by following gene expression dynamics of engineered circuits in bacterial cells or labeled proteins in yeast, mathematically using stochastic differential equations, and computationally using Gillespie simulations (Levchenko and Nemenman, 2014). Theoretical, modeling work and intuition suggest that a variety of parameters, from mRNA and protein degradation rates to chromatin accessibility, can influence PoV. However, the environmental, cellular, and biochemical conditions affecting the extent of PoV remain poorly understood, particularly in mammalian cells that often exhibit complex signaling and gene-regulatory mechanisms.

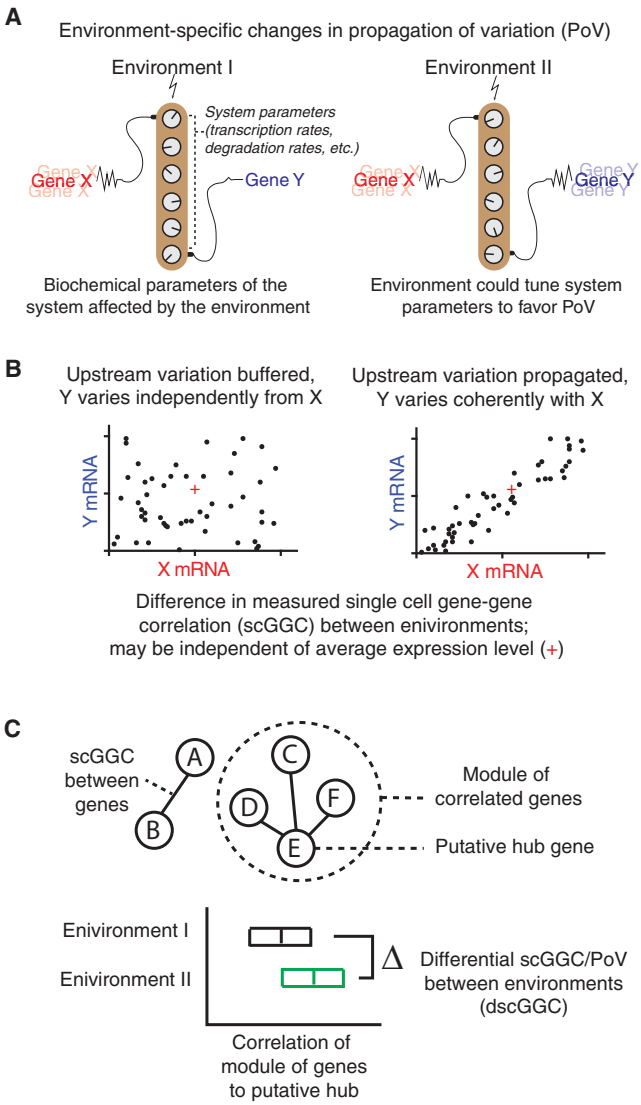

Figure 1. Assessing Condition/Environment-Dependent Propagation of Variation

(A) A regulatory connection between two genes (such as a transcription factor X that binds to the enhancer/promoter region of a target gene Y to regulate the transcription of the target gene) could have different degrees of "activity" (e.g., active versus inactive) depending on the environmental context. The environmental context could affect biochemical parameters governing the expression of and interaction between X and Y, and could hence affect the quantitative extent of propagation of variation (PoV) between the two genes within cells.

(B) PoV between two genes can be inferred from the degree of their correlation among single cells in the cell population. Thus, differences in PoV between the two conditions can be detected as changes in the strength of single-cell gene-gene correlations (scGGCs). Such correlation changes may or may not be associated with average expression.

(C) Since genes function in larger regulatory networks within cells, changes in the value of parameters governing PoV among genes could result in modules of genes showing differential scGGCs (dscGGCs) among conditions. In particular, certain "hub" genes, such as transcription factors that regulate and thus can propagate expression variation to multiple downstream target genes, may exhibit dscGGCs with many of its targets.

PoV between genes can be detected as correlation in gene expression among single cells in a cell population (Dunlop et al., 2008; Pedraza and van Oudenaarden, 2005; Stewart-Ornstein et al., 2012). Recently, multiplexed single-cell profiling using approaches such as microfluidic qPCR and single-cell RNA sequencing (RNA-seq) revealed that such single-cell based gene-gene correlations (scGGCs) are prevalent, and efforts are underway to reconstruct the topology of gene networks by utilizing scGGCs (Pina et al., 2015). Context-dependent PoV behavior among genes could in principle be revealed by comparing the degree of scGGCs in cell populations exposed to distinct environments. This approach utilizes the environment as a natural perturbation of multiple biochemical parameters (such as chromatin accessibility and phosphorylation activity) simultaneously regulating PoV. The combined effects generated by such natural perturbations would be difficult to achieve by a priori selecting and perturbing one parameter at a time. By linking changes in scGGCs to those in signaling, chromatin, and transcriptional activities among environments, we can begin to explore the biochemical underpinnings of scGGCs and PoV.

Here we employ four different cytokine perturbation environments to systematically study environment-dependent PoV in human macrophages. Macrophages provide an attractive mammalian model for studying PoV across environments as they are capable of diverse phenotypic adaptations and have been implicated in many human diseases (Murray and Wynn, 2011). Generation and integrative analysis of both single-cell and "stochastic profiling" (Janes et al., 2010) data revealed significant differences in PoV under distinct conditions of cytokine exposure. Our work illustrates how natural perturbations can be utilized to reveal adaptive PoV behavior and suggests that tuning of PoV in gene-regulatory networks may occur via post-translational and chromatin-mediated mechanisms to drive or buffer expression co-variation among genes in single cells. Such tuning may be a widespread feature of cellular adaptation to diverse environments and can shape environment-dependent patterns of cellular heterogeneity.

RESULTS

Environment-Dependent PoV

We sought to examine how PoV may change in an environment-dependent manner. While observing scGGCs is often expected when a gene X is capable of regulating another gene Y, it is possible that cells may tune PoV, for example to attenuate PoV when buffering of stochastic fluctuation in gene expression level is beneficial, or to enhance PoV when robust transmission of upstream signals is desired (Figure 1A). Changes in PoV could change the co-variation of gene expression among single cells and thus also the pattern of cellular heterogeneity in the population (Figure 1B). As certain "hub" genes may regulate many partners, changes in PoV involving hubs may lead to modules of genes showing differential scGGC between different environments (Figure 1C).

To begin to explore environment-dependent PoV, we performed in silico stochastic simulations of a simple, prototypical two-gene cascade model consisting of a TF (X) regulating a target gene (Y) in single cells across multiple randomly selected sets of parameter combinations, with each parameter

combination representing a different environment that perturbs multiple parameters at once. Confirming our intuitions, these simulations revealed that the strength of PoV between two genes can be tuned by the biochemical parameters governing their expression and interaction, and high PoV only occurs for specific parameter combinations such as those permitting a sufficiently high rate of degradation of protein X and rate of interaction of protein X with the promoter/enhancer of gene Y (Figure S1 and Table S1).

Cell-to-Cell Variation Can Be Robustly Detected in Macrophages under Multiple Environmental Conditions

To utilize natural environmental perturbations of cells to study the effect of altering multiple biochemical parameters on PoV, we used human macrophages, an immune cell type known for its phenotypic and functional diversity (Gordon and Taylor, 2005). Environmental adaptations of macrophages, particularly their tissue-dependent behavior and in vitro responses to cytokines or bacterial products such as tumor necrosis factor alpha (TNF-α), lipopolysaccharide, interferon γ (IFN-γ), or interleukin-4 (IL-4), have been productively studied at the transcriptomic, signaling, and epigenomic levels (Schultze and Schmidt, 2015). We obtained single-cell expression profiles from human blood monocyte-derived macrophages cultured in four conditions: (1) baseline (CNT), (2) after stimulation for 24 hr using IFN-γ in conjunction with TNF-α (IFN + TNF), (3) 24 hr post IL-4 stimulation, and (4) 24 hr post IL-10 stimulation. The latter three conditions are intended to model, respectively, the cellular state in inflammatory, anti-parasitic, and regulatory environments (Murray and Wynn, 2011).

We sorted single cells using indexed fluorescence-activated cell sorting into 96-well plates followed by microfluidic-based multiplexed qPCR transcript profiling (Figure 2A). Our flow cytometric and qPCR panels measure genes associated with macrophage activation (e.g., *CD36*, *CD206*, *STATs, PPARG*), genes known to function in core cellular and metabolic processes, as well as genes selected based on publicly available gene expression compendia of activated macrophages and human immune cells (Figure 2B).

We observed widespread cell-to-cell heterogeneity among macrophages harvested from the same culture. Namely, cells exposed to the same environment exhibited markedly different transcriptional profiles (Figure 2C; expanded heatmap in Figure S2A). IFN + TNF-treated cells had clearly distinct expression profiles from the other three treatments (Figures 2C and 2D). By contrast, even though changes were clearly apparent after IL-10 or IL-4 treatment, including upregulation in surface protein marker expression (e.g., CD163 in IL-10; CD206 in IL-4; Figure 2E), cells in these conditions were less separable based on mRNA expression from each other and from those in CNT, likely owing to the overall milder changes in average expression and extensive cell-to-cell heterogeneity in these conditions. Many genes had bimodal expression patterns within the same treatment condition: one mode corresponds to cells with undetectable levels of expression (“OFF” cells), while the other reflects the continuous differences among cells expressing detectable levels of the transcript (“ON” cells). This bimodal pattern was unlikely due to the presence of cells that failed to detect the cytokine treatment since phospho-flow analysis of cells harvested from each treatment condition exhibited activation of the expected canonical signaling pathways (Figure 2F). Visualization of cells in dimensionality-reduced space based on gene expression for each condition independently also did not reveal any clearly distinct clusters of cells (Figure S2B).

Since technical noise can be large in single-cell mRNA measurements (Grün et al., 2014), we next adopted stochastic profiling (Bajikar et al., 2014; Janes et al., 2010), by repeatedly profiling samples of ten random cells for all four conditions (Figure S2C). This process provides information about the underlying single-cell expression distribution but is less prone to technical noise than direct single-cell profiling due to a 10-fold increase in the average amount of input RNA (Janes et al., 2010). A comparison of the mean expression of single cells with that of the ten-cell samples (divided by ten) showed that for most gene/condition combinations with moderate to high expression, single- and ten-cell samples are largely concordant. For lowly expressed gene/condition combinations, ten-cell data shows better detection sensitivity, as expected (Figure S2D). To better understand the prevalence of true versus technically induced false OFFs in the single-cell data, we applied a Bayesian method we developed (QVARKS; Narayanan et al., 2016) to integrate both single- and ten-cell data, and found that only a few gene-condition combinations suffered from large technical detection problems (Figure S2E; e.g., *CD36* in IL-4 condition). Consistent with our observations using only single-cell data, this analysis revealed that expression heterogeneity originated primarily from ON versus OFF cells and from continuous expression differences among ON cells (Figures S2F and S2G). Thus, macrophages under distinct environments exhibit substantial cell-to-cell variations. Although the ultimate origin of this heterogeneity is not known, we can utilize these robust variations to assess condition-dependent scGGCs and PoV.

Environment-Dependent scGGCs and PoV in Human Macrophages

To assess scGGCs within each stimulation condition, we chose to use the ten-cell data (Table 1; step 1), which robustly captures scGGCs computed from single cells from the same population (Bajikar et al., 2014) (Figures S3A and S3B). Importantly, we uncovered many more significant correlations using ten-cell data (Figures S3A and S3B), likely reflecting the improved robustness of ten-cell measurements. Both discrete- and continuous-type correlation present in the single-cell data could be found as continuous correlations in the ten-cell data (Figure 3A). Thus, ten-cell data provide a robust readout of both single-cell variation and scGGCs. The scGGCs were also largely unaffected by correction for differences in cell size (see STAR Methods and Figure S3C), indicating that this known extrinsic factor was not driving these observations.

We assessed the replicability of the detected correlations using additional ten-cell data obtained from two independent experiments on sorted cells derived from the same donor. The significant gene-gene correlations we detected earlier exhibited significant replication (Table S2, $p < 0.05$ for replication for each condition in each experiment, with IL-10 and CNT conditions exhibiting the most significant replication). We next assembled gene-gene correlations detected in the discovery and at least one of the two replication experiments to build scGGC networks

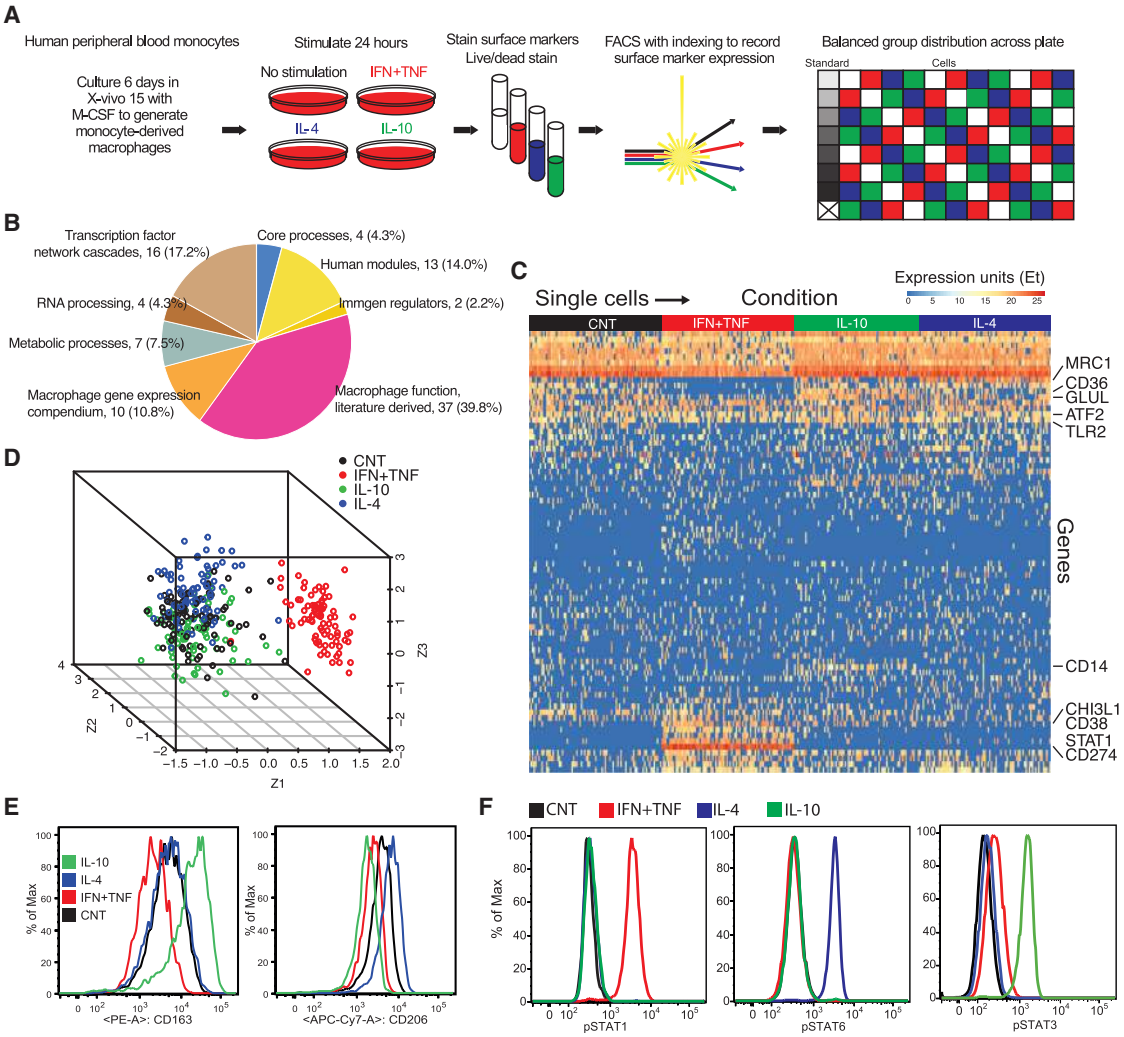

Figure 2. Robust Gene Expression Heterogeneity in Macrophages Provides the Substrate to Study PoV

(A) Experimental setup of single-cell macrophage analysis. Macrophages differentiated in vitro from human blood monocytes using M-CSF are treated with different cytokines for 24 hr, followed by surface marker labeling, indexed single-cell sorting, and balanced profiling of samples from different conditions in each of the Fluidigm qPCR plates.

(B) Functional category distribution of genes in our Fluidigm qPCR panel.

(C) Gene expression profiles of single cells obtained from the same donor and exposed to the indicated treatments. Heatmap shows the expression levels in Et units (40-Ct, normalized across plates) of single cells (columns) sorted from the indicated treatment conditions. Only genes that have at least 10% of cells having non-zero expression (i.e., "ON") in at least one treatment condition are shown (77 of 93 measured genes). See also Figure S2A.

(D) Visualization of single-cell gene expression profiles in reduced dimensions. Each dot is a single cell, and the 77 genes shown in (B) are reduced to three dimensions (or factors) by using zero-inflated factor analysis (Pierson and Yau, 2015). See also Figure S2B.

(E) Selected surface marker phenotype of macrophages in the indicated treatment conditions as measured by flow cytometry.

(F) Phosphorylation status of canonical STAT signaling proteins under the cytokine treatment doses used (data from a representative experiment shown [out of a total of two experiments]).

representing the underlying co-variation of gene expression among cells in each condition (Figure 3B; see STAR Methods and Data S1). Shared patterns of scGGCs among conditions were observed, such as that between *CREG1* and *FTL*, *CASP3*, and *IFI30*. These interactions could reflect PoV in a core network that operates in macrophages independent of the environment, given that *CREG1* was predicted as a transcriptional regulator of core macrophage-associated genes in mouse cells (Gautier et al., 2012). Some scGGCs also appeared to be condition-specific. For example, correlations involving *CD274* were higher in the IFN + TNF condition, which may be because *CD274* has higher expression in IFN + TNF (Table S3) and a substantially higher fraction of cells had detectable *CD274* expression in that condition (Figure 2C).

An interesting feature of these networks is the presence of modules of genes that appeared correlated to each other either directly or indirectly through hub genes in a condition-dependent manner. To test whether some of these differences across

Table 1. Systematic Identification of the Extended ATF2 dscGGC Module

Step	Description
1. Compute scGGC network in each condition.	1a. Perform integrative analysis of single/ten-cell data, and identify genes with sufficient detects and hence robust cell-to-cell variation in each condition (Figures 2 and S2). 1b. Compute ten-cell Spearman correlation for each pair of genes to construct scGGC networks within each condition, after verifying that single- and ten-cell correlations are broadly concordant (Figures 3 and S3).
2. Compute dscGGC (differential scGGC) in each pair of conditions.	2a. Use scGGC networks to select hub/partner gene modules for testing dscGGC when comparing two conditions; use the first two ten-cell experiments to choose the FDR cutoff of these scGGC networks, and the unseen third ten-cell experiment to perform the final replication test. 2b. Test each module for statistically significant dscGGC signal (i.e., statistically significant gain or loss of correlation strength in one condition relative to another).
3. Identify the most replicated dscGGC modules using all three ten-cell experiments, and TF binding motif enrichment based on H3K27ac enhancer profiling.	3a. Identify condition pairs with independent replication of dscGGC signals: IL-10 versus CNT pair satisfied this criteria (Figure S3), and resulted in seven replicated dscGGC modules (Figures 3 and S3). 3b. Merge the four largest of these seven dscGGC modules since they had overlapping genes. As this merged module was enriched for ATF2/AP-1 binding motif in nearby enhancers with activity (H3K27ac) marks, call it the extended ATF2 dscGGC module (Figure S3). Also use H3K27ac data in IL-10 versus CNT (Figure S4) to select enhancer regions for follow-up by ChIP-qPCR (Figures 4 and S4).

conditions are indeed statistically significant (Table 1; step 2) and not an artifact of the cutoffs used to construct/visualize these networks, for each gene (as a potential correlation hub) we used a bootstrap/resampling-based procedure to assess whether the correlation strength between this potential hub gene and other partner genes, in aggregate, in one condition is significantly different from those in another condition. Testing for differential correlation for each scGGC between two conditions will have increased statistical uncertainty beyond detecting scGGCs in a single condition; here we have increased statistical power by testing for differences in correlation at the gene module level rather than at the level of each gene-gene correlation, which is also more robust against experimental noise compared with assessing individual scGGCs. Consistent with IL-10 and CNT scGGCs exhibiting the most significant replication as reported above, this analysis revealed seven genes showing hub-like differential scGGC/PoV (dscGGC) with their partners in the IL-10 versus CNT comparison (false discovery rate [FDR] < 0.1 cutoff in the primary ten-cell experiment followed by replication in two independent ten-cell experiments at $p < 0.1$; Figure S3D; see also Table S4); while other condition comparisons yielded some dscGGC hits (see Table S4), they lacked the overall significant replication signal found for IL-10 versus CNT and were thus not further considered (see STAR Methods).

Hubs exhibiting dscGGCs with at least ten partner genes in the IL-10 versus CNT comparison include *ATF2*, *CASP1*, *GLUL*, and *HIF1A* (Figure 3C). The correlated gene partners for these hub genes are highly overlapping, and thus they can be considered together as a larger, merged gene module exhibiting higher PoV/scGGCs in the IL-10 condition relative to CNT (Figure S3E). Of the four IL-10-specific dscGGC hubs, *ATF2* and *HIF1A* are known to encode TFs, and hence are candidates to directly regulate the expression of their partner genes. To assess whether ATF2 or HIF1α may directly regulate genes in the larger merged module, we generated histone H3 lysine 27 acetylation (H3K27ac) chromatin immunoprecipitation sequencing (ChIP-seq) data for both CNT- and IL-10-treated macrophages to identify enhancer/promoter peaks nearby module genes (Creyghton et al., 2010). Based on motif enrichment in the union of peaks found in CNT and IL-10 near module genes, enrichment was found for the AP-1 motif bound by ATF2 ($p = 1.41 \times 10^{-56}$), while no enrichment was found for HIF1α ($p > 0.9$, relative to genomic background; p values from the threshold-free log-normal distribution based-enrichment test provided in the PWMEnrich package; see STAR Methods). The detection of a potential IL-10-specific role of *ATF2*, a member of the AP-1 TF complex, is particularly intriguing: despite IL-10 being classically thought of as an anti-inflammatory activator and *ATF2* as activated downstream of inflammatory signals such as lipopolysaccharide (Liu et al., 2009; Murray, 2006), our results showed that *ATF2* exhibited significant dscGGCs in IL-10-treated cells rather than in the inflammatory condition IFN + TNF (Figure 3B). We hereafter refer to the larger gene module from the merged sets of these four dscGGC hubs as the "ATF2 extended module" (Figure S3E and Table 1; step 3).

In principle, changes in scGGCs between different conditions may occur without overt changes in average expression measured at the cell population level (Figure 1). In support of this notion, many genes in the ATF2 extended dscGGC module in IL-10 versus CNT were not differentially expressed based on average expression obtained from ten-cell data (Table S3B; Figure S3F shows average fold change of genes in the ATF2 extended module, based on ten-cell data). To further assess the relationship between dscGGCs and average expression estimated from multiple donors through an alternate profiling technology, we utilized bulk RNA-seq data that we generated from CNT- and IL-10-treated cells in a related study (our unpublished data; data available at NCBI GEO: GSE81444). As a group, the extended module genes exhibited statistically indistinguishable change after IL-10 treatment relative to CNT when compared with that of a set of "negative controls," which is comprised of genes from our qPCR panel that were not correlated to ATF2 in the IL-10 treatment and were not part of the ATF2 extended module ($p = 0.8469$, Wilcoxon test, Figure S3G; see STAR Methods

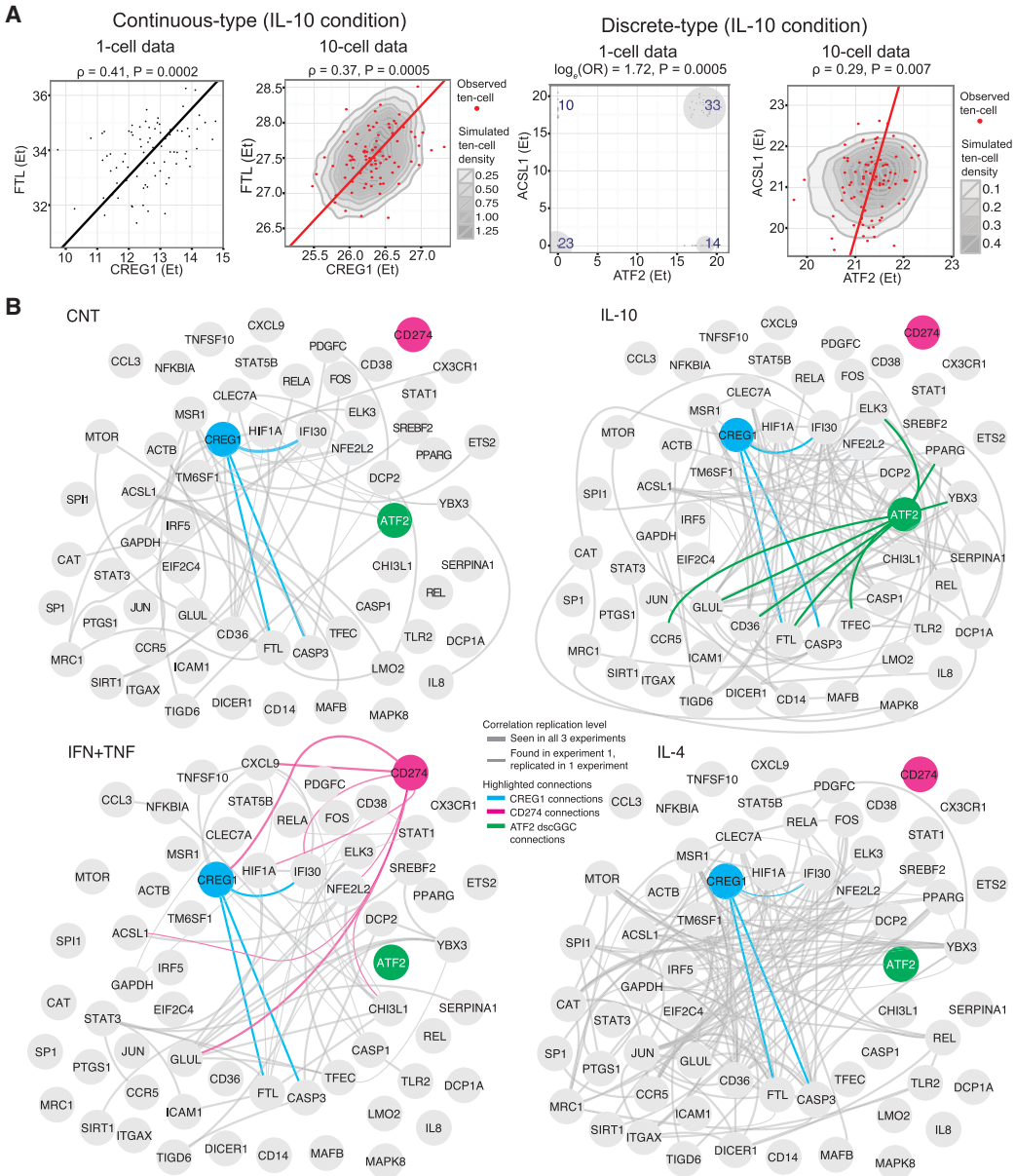

(legend on next page)

for the negative control gene set selection procedure). We also note that for the negative control genes no significant association was detected between the changes in their correlation strength with ATF2 and the changes in their average expression between the IL-10 and CNT conditions ($p > 0.1$ for all three experiments; Spearman correlation test; Figure S3H); thus, increased expression and hence increased sensitivity to detect changes in correlations between IL-10 and CNT alone is unlikely to explain the increased correlations we observed among genes in the ATF2 module in the IL-10 relative to CNT condition.

Molecular Basis of IL-10-Dependent PoV

We next explored the potential molecular mechanisms driving condition-dependent PoV by focusing on the ATF2 extended module in IL-10 versus CNT conditions. PoV/scGGC tuning may involve altering the degree of interactions between the upstream regulator, postulated to be ATF2 in this case, and the enhancer/promoter of its regulated genes. To explore this possibility, we examined the activity of enhancers bearing ATF2 binding motifs using the H3K27ac ChIP-seq data introduced above and also the levels of bidirectional enhancer RNAs (eRNAs) measured by Cap Analysis of Gene Expression (CAGE; Andersson et al., 2014). Overall, the H3K27ac or eRNA peaks that contained predicted AP-1/ATF2 binding sites nearby the dscGGC genes have very mildly elevated signal compared with the non-dscGGC-negative control genes ($p = 0.075$ for H3K27ac peaks, $p = 0.049$ for eRNA peaks, Figures S4B and S4C), suggesting increased enhancer activity at these sites after IL-10 treatment.

To assess whether IL-10 treatment also induced ATF2 binding to putative AP-1 motif-containing sites within promoter/enhancer peaks near ATF2 extended module genes, we used genome-wide ATF2 ChIP-seq data to predict individual ATF2 binding sites within a set of select enhancer peaks (see STAR Methods for selection criteria, including the criterion used for selecting peaks having higher H3K27ac signal in cells treated with IL-10 compared with CNT condition). We then used ATF2 ChIP-qPCR to validate whether these predicted sites indeed exhibit ATF2 binding and have quantitatively higher ChIP signal in IL-10 than in CNT. Compared with background regions not containing ATF2-binding motifs, the predicted ATF2-binding regions have substantially higher signal in both conditions (Figure 4A, $p = 3.8 \times 10^{-5}$ and 4.996×10^{-5}, respectively, in IL-10 and CNT, F test comparing two nested linear models after accounting for donor/region effects as described in STAR Methods). While the signal from the background control genomic regions was not different between CNT and IL-10 conditions, the predicted sites exhibited higher signal in the IL-10 condition ($p = 9.209 \times 10^{-5}$, F test as above; Figure 4A). The ATF2 ChIP signal for the predicted sites was also higher in IL-10 than in CNT when the data are expressed as fold enrichment values against background ($p = 1.996 \times 10^{-6}$, F test as above; Figure 4B). Together, these data suggest that quantitatively increased interaction between ATF2/AP1 and enhancers/promoters nearby dscGGC genes is a potential contributor to the gain of correlation between ATF2 and dscGGC genes following IL-10 activation.

Increased interaction between ATF2 and enhancers in the IL-10 condition could reflect better enhancer accessibility facilitated by chromatin regulatory factors and/or higher levels of active ATF2/AP-1. Like many TFs, the activity of ATF2 is regulated by phosphorylation through kinase signaling cascades in the cytoplasm, which promotes ATF2 translocation to the nucleus and its DNA binding activity (Lau and Ronai, 2012). Thus, despite the fact that IL-10-treated cells only showed mildly elevated average *ATF2* mRNA expression versus CNT (1.2-fold increase, $p = 3.94 \times 10^{-5}$, Wald test by DESeq2; Figure S3G), the activity of ATF2, as indicated by the amount of phosphorylated ATF2 in the nucleus, could be different between the two conditions. To test this hypothesis, we first assessed Thr71 phosphorylation of the ATF2 protein (pATF2). Phospho-flow experiments indicated a non-zero baseline pATF2 signal in CNT conditions and a mild, rapid increase in median pATF2 levels post IL-10 activation (Figure 4C), which peaked at 2 hr and remained elevated at 24 hr, the same time point at which our single- and ten-cell transcript profiling data were collected. The pATF2 induction dynamics followed that of pSTAT3, the canonical STAT downstream of IL-10 activation via the IL-10 receptor (Figure 4C, lower panel); and pATF2 induction following IL-10 activation was consistently observed in multiple independent experiments (Figure 4D, $p = 0.0061$, paired t test). Staining with an antibody against total ATF2 protein showed similar or slightly reduced average levels of total ATF2 after 24 hr of IL-10 treatment (Figure S4D), consistent with the mild bulk fold change in *ATF2* mRNA expression. Together, these data suggest that the observed elevation in pATF2 level in IL-10 versus CNT can be attributed to a higher ATF2 phosphorylation rate (or a lower rate of dephosphorylation) rather than to increases in the average expression of the ATF2 protein.

Consistent with the increase in pATF2 observed by flow cytometry, confocal imaging revealed increased nuclear pATF2 24 hr after IL-10 activation, after accounting for changes in nuclear size, and these data also highlight the cell-cell heterogeneity in nuclear pATF2 levels in each condition (Figures 4E and 4F, $p = 6.6 \times 10^{-7}$, t test). While other mechanisms may be involved,

Figure 3. Systematic Identification of scGGC Networks and Differential scGGC (dscGGC) Hubs and Gene Modules

(A) Concordance between discrete/continuous single-cell GGCs and continuous ten-cell GGCs for two example gene pairs. Simulated ten-cell GGCs shown as 2D contour density (in gray) are computed using the single-cell data only (see STAR Methods). See also Figures S3A and S3B. ρ, Spearman correlation; OR, Odds Ratio.

(B) Within each treatment condition, scGGC networks are assembled based on individual gene-gene correlations (i.e., edges in the network) computed using the "discovery" ten-cell dataset passing the false discovery rate < 0.2 cutoff. Thickness of edges indicate the extent of replication in additional validation experiments. Genes and edges discussed in the text are highlighted in color. Note that nodes are fixed in the same relative position for each network. See also Figure S3C.

(C) The four dscGGC hubs with the largest number of partner genes identified in the IL-10 versus CNT comparison, which were then combined to form the ATF2 extended module. The Spearman correlation coefficients between the hub gene (e.g., *ATF2* in the first panel) and partner genes are shown for the IL-10 and CNT conditions as boxplots (see STAR Methods). For each hub gene and its associated gene module, dscGGC p value from the bootstrap procedure (see STAR Methods) is shown after adjustment for the discovery experiment (Exp. 1) and as is for the two validation experiments (Exp. 2 and 3). See also Table S4, and Figures S3D and S3E.

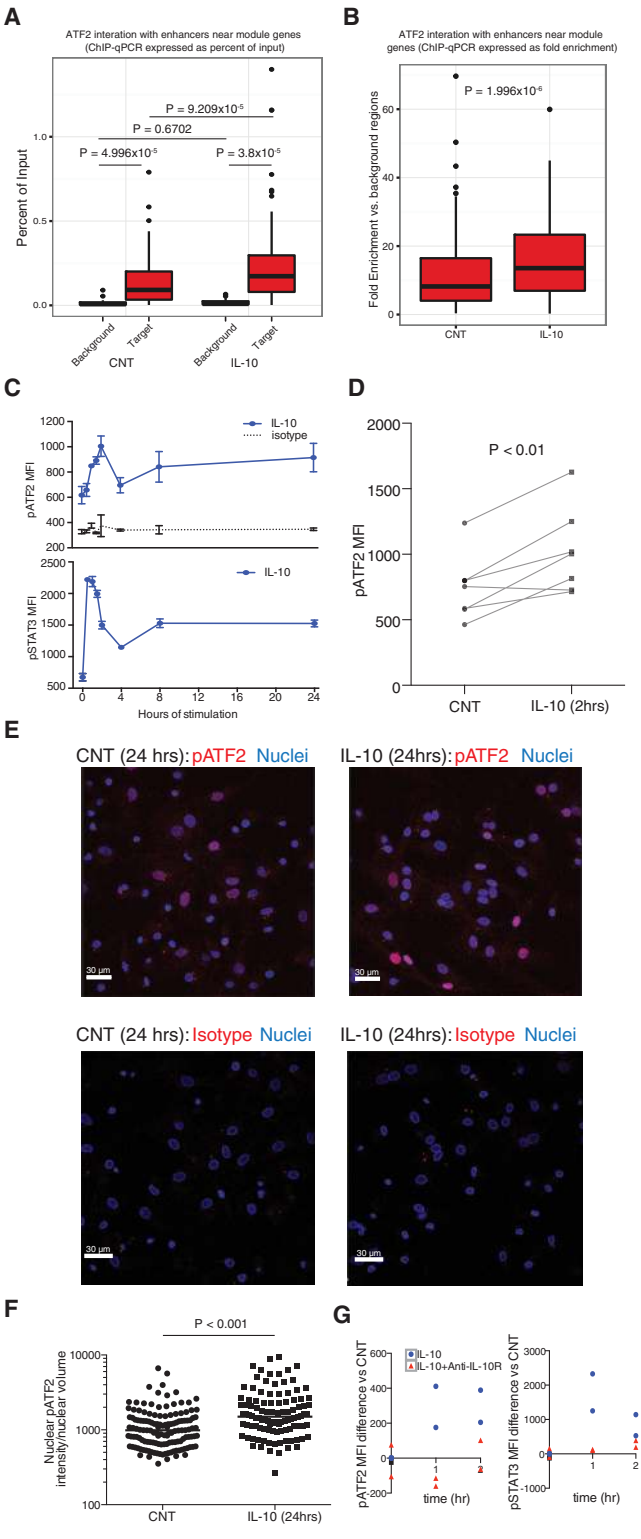

Figure 4. Changes in Chromatin Interaction and Protein Activation Are Associated with Enhanced PoV in the ATF2 Extended Module after IL-10 Treatment

(A and B) ATF2 ChIP-qPCR data (expressed as percent of input or fold enrichment, respectively) was used to evaluate binding of ATF2 to select H3K27ac peak regions near ATF2 dscGGC extended module genes in CNT and IL-10 environments. Data are obtained from three independent ChIP experiments using cells from three donors for 14 target and four background regions. The p values are based on F test comparing two nested linear models after accounting for donor and target region effects (see STAR Methods).

(C) pATF2 and pSTAT3 induction dynamics following IL-10 treatment. Representative of two independent experiments. The plot shows mean ± SD of replicate samples from one experiment. See also Figures S4D and S4E.

(D) pATF2 induction at 2 hr following IL-10 treatment from seven independent experiments using cells from four different donors is shown (paired data from each experiment is connected by a line). The p value was obtained from paired t test.

(E and F) Nuclear pATF2 staining 24 hr post IL-10 treatment measured using confocal imaging. Each dot in (F) corresponds to the level of pATF2 staining intensity in a single nuclei after normalization by nuclear size delineated by DAPI co-staining. Multiple fields of view are combined; data shown are from one experiment, and are representative of two experiments utilizing cells from different donors. The p value shown in (F) was obtained from Student's t test.

(G) pATF2 and pSTAT3 induction dynamics after IL-10 treatment in the absence/presence of an IL-10 receptor-blocking antibody. Points represent data from three independent experiments, measured at 1 hr, 2 hr, or both time points. Values shown correspond to changes in median fluorescence intensity (MFI) relative to the non-treated cells (baseline).

these data provide evidence that the increased interaction between ATF2 and the enhancers of dscGGC genes in IL-10 compared with CNT conditions can be attributed, at least in part, to elevation in ATF2 phosphorylation and nuclear localization. Interestingly, the non-zero level of pATF2 in both IL-10 and CNT conditions (according to both phospho-flow and imaging, based on comparison with antibody-isotype control stained cells; Figures 4C and 4E) suggests that the increased enhancer interactions result from fine-tuning of ATF2 phosphorylation rather than "digital" ON/OFF switching of ATF2 activity. In addition, the large cell-to-cell variation in the extent of pATF2 nuclear localization (Figures 4E and 4F) further supports the hypothesis that ample variation exists in the TF activity of ATF2 at the single-cell level in both conditions, but such variation was transmitted more effectively to downstream genes in the IL-10 than in the CNT environments.

To test whether the phosphorylation of ATF2 was a direct downstream effect of IL-10 ligation to its receptor, we stimulated macrophages using IL-10 together with an IL-10 receptor-blocking antibody and then assessed pSTAT3 and pATF2 levels (Figure 4G). In the presence of the blocking antibody, both pSTAT3 and pATF2 were not elevated, thus confirming that the activation of ATF2 was a direct effect of IL-10 and not due to reasons such as activation by other agents in the cytokine preparation. Although the mechanism by which the IL-10 receptor mediates the phosphorylation of ATF2 is unclear, the level of pATF2 was found to be significantly correlated with that of pSTAT3 among single cells following IL-10 activation, even after accounting for cell size via linear modeling (Figure S4E; $p < 2 \times 10^{-16}$ at 2 and 24 hr after IL-10 treatment, see STAR Methods for methodological details), further suggesting that ATF2 may be linked to the IL-10 receptor-mediated signaling pathway.

IL-10 has been proposed to play an anti-atherogenic role and can increase both cholesterol uptake and efflux in macrophages (Han and Boisvert, 2015). Several of the genes correlated with *ATF2* specifically in the IL-10 condition, including *CD36* and *MSR1* (both receptors mediating uptake of low-density lipoprotein), *TLR2, PPARG,* and *MAFB,* have been linked to

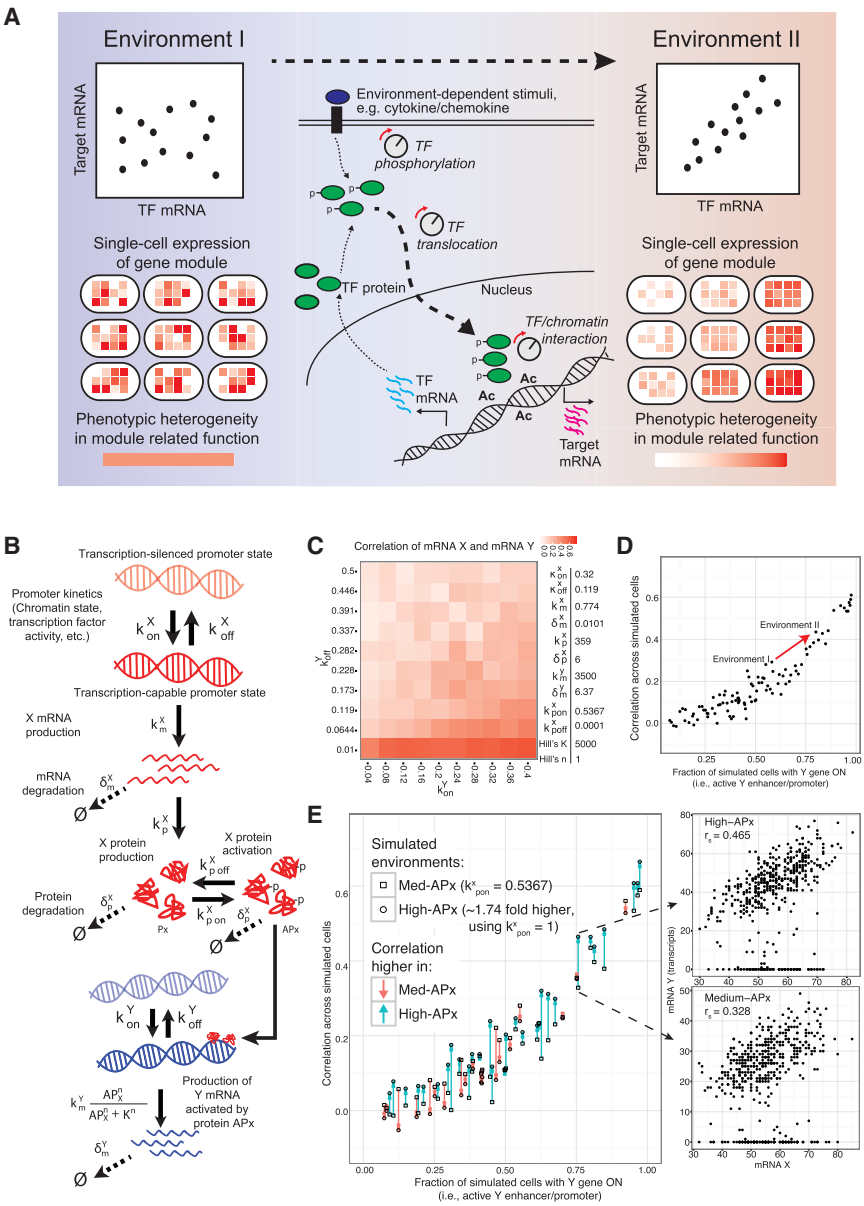

Figure 5. Proposed Model and Stochastic Simulation of Condition-Dependent PoV

(A) Our results suggest a model where environment-dependent scGGCs/PoV between an upstream factor and downstream target genes is achieved by tuning the degree of phosphorylation or translocation of the factor and enhancer activity nearby the targets. Context-dependent PoV could potentially lead to functional diversification among cells in the population, with for instance increased PoV resulting in coordinated expression of functionally related genes in a module.

(B) Modeling schematic of a two-gene-regulatory cascade in which the activated protein product of gene X regulates the transcription of gene Y. mRNA and protein are abbreviated respectively with "m" and "p" subscripts in the parameter names.

(C) A color map of scGGC values (computed among single cells in a simulated cell population at a fixed, "snapshot" time point) is shown as a function of different combinations of activation (ON) and deactivation (OFF) rates of the Y promoter (corresponding to $\kappa^Y_{on}, \kappa^Y_{off}$ values in Figure S1D, respectively). Values used for other parameters are listed alongside the plot. Units of parameters are events/hr or events/hr/molecule as in Figure S1D.

(D) Different representation of (C) where the fraction of simulated cells with accessible promoter/enhancer at the fixed snapshot estimated by $\kappa^Y_{on}/(\kappa^Y_{on}+\kappa^Y_{off})$ is shown along the x axis and scGGC is shown along the y axis.

(E) Assessing changes in scGCC by increasing the activation rate of protein X and hence the average level of active protein X (AP_X) in silico, simulated over different combinations of Y promoter/enhancer accessibility, achieved by considering every κ^Y_{off} value shown in (C) with every other κ^Y_{on} value in (C) for better clarity. Two environments are simulated, High-AP_X and medium-AP_X (Med-AP_X) conditions, with arrows connecting the paired AP_X conditions for each κ^Y_{on} and κ^Y_{off} combination (where the only difference is the protein X activation rate; the color of the arrow indicates if the mRNA X-Y correlation is higher in the Med-AP_X or the High-AP_X condition). For a selected parameter set, the inset panel shows a scatterplot of mRNA X and Y transcript levels in each simulated cell and associated Spearman correlation r_s (at a fixed snapshot time point, see STAR Methods).

atherosclerosis (Hamada et al., 2014; Moore et al., 2013; Zhang and Chawla, 2004). Ingenuity pathway analysis of the ATF2 extended module genes revealed connections between many of the these genes and lipid metabolism-related pathways (Figure S4F), and H3K27ac peaks detected in this study nearby several of the extended module genes harbor genetic variants known to be associated with lipid/metabolic traits based on genome-wide association studies (GWAS) (Table S5). Further supporting a link between this group of genes and atherosclerosis, comparison of the expression of genes in both the ATF2 module and the extended module using two external microarray datasets of atherosclerosis plaque macrophages revealed that the module genes tended to be more differentially expressed than the negative control gene set in plaque macrophages compared with other control cell types (Figures S4G and S4H).

Proposed Model and Its Quantitative Assessment via Stochastic Simulations

Our experiments reveal that environment-dependent, quantitative tuning of chromatin-TF interactions near genes in the *ATF2* module can modulate their PoV behavior (Figure 5A). Specifically, by increasing the average rate of phosphorylation (or decreasing the rate of dephosphorylation) and nuclear localization of ATF2, the IL-10/IL-10R signaling pathway may serve to further open up the "channel" for the propagation of *ATF2* transcript variability to downstream genes (Figure 5A). For example, comparing with a cell in CNT, an IL-10-treated cell expressing similar levels of the *ATF2* transcript tends to have a higher level of nuclear pATF2, which potentially has a better capacity to interact with the enhancer/promoters of downstream partner genes. This is supported by the elevated ATF2 ChIP-qPCR,

H3K27ac, and eRNA signals nearby partner genes in the IL-10 environment. Consistent with this notion, the subset of genes in the ATF2 extended module whose enhancers/promoters were selected for ChIP-qPCR testing and thus exhibited experimental evidence of ATF2 binding show mildly increased average mRNA expression compared with the negative control set ($p = 0.0067$, Wilcoxon test; Figure S5A; see STAR Methods for selection criteria). Elevated H3K27ac and eRNA signals could be a result of ATF2 binding or factors other than *ATF2* acting independently or in conjunction with *ATF2* to increase activity of the promoter/enhancer region near partner genes post IL-10 treatment. As these effects are rendered over cells in the population expressing different levels of *ATF2*, increases in scGGCs between the mRNA of *ATF2* and that of its partner genes in IL-10 relative to CNT could emerge (Figure 5A), which may then lead to heterogeneity in the module-related phenotype among cells in the IL-10 condition.

To assess whether key features of this proposed model are quantitatively consistent with our experimental observations, we next simulated an augmented version of the prototypical two-gene cascade model (gene X regulates gene Y) evaluated earlier in Figure S1. To capture the activation of a protein via post-translational modification (phosphorylation) and subsequent nuclear translocation as in the case of ATF2, we added an activation and a corresponding deactivation reaction for protein X, where only the activated form can affect the transcription of gene Y (Figure 5B). We then assessed via in silico stochastic simulations if increase in scGGC is observed after: (1) increasing the accessibility or activity of enhancers/promoters of gene Y (modeled as having higher ON rate and/or lower OFF rate values [κ^Y_{on} and κ^Y_{off} in Figure 5B]), as suggested experimentally by the increase in H3K27ac and CAGE signals near promoters/enhancers of the *ATF2* partner genes in the IL-10 relative to CNT condition; and (2) increasing the activation rate of the upstream protein X and thereby the average level of active protein X by 1.74-fold, given that the average level of the phosphorylated, nuclear ATF2 protein in the IL-10 condition was 1.74-fold higher relative to the CNT condition (Figure 4F).

Our simulations confirmed that increasing the accessibility of Y promoters/enhancers alone can lead to increases in scGGC and hence in PoV (Figures 5C and 5D). Note also that in general, the Y promoters/enhancers have to frequently reside in the "active" state in order to achieve high PoV (see κ^Y_{on} and κ^Y_{off} plots in Figure S1D). Increasing the activation rate of protein X by the set amount can also increase scGGC across a range of Y promoter/enhancer accessibility scenarios (Figure 5E). These observations are robust under alternate modeling setups, such as when the activated form of protein X not only influences transcription initiation of gene Y, but also affects accessibility of the Y promoter/enhancer (as modeled by having κ^Y_{on} depend on the level of active protein X; see STAR Methods) (Figures S5B and S5C). Furthermore, given a combination of biochemical parameters that can generate high scGGC (Spearman correlation > 0.7 as in Figure S1C), increasing the activation rate of protein X alone tends to further elevate the strength of the correlation (Figure S5D). Together, these simulation results further strengthen key features of our proposed model, including the notion that tuning the promoter/enhancer accessibility and/or the upstream protein's activation can markedly influence PoV.

DISCUSSION

Our analysis of single-cell gene-gene correlation in human macrophages exposed to distinct environments lends concrete experimental support to the notion of environment-dependent regulation of PoV, and highlights the potential role for contextually triggered differences in phosphorylation, nuclear localization, and enhancer statuses in tuning PoV. While these processes are commonly appreciated to be involved in signal transduction and cellular adaptation to different environments, their role in adaptively regulating PoV and thus patterns of cellular heterogeneity from a single-cell biology perspective, was not well known and appreciated. Our results suggest that the propagation of single-cell variations may be regulated across different environments through fine-tuning of key gene-regulatory network parameters that govern the sensitivity of downstream genes to the fluctuations in the upstream regulator.

Environment-dependent regulation of PoV is needed given the diverse, complex niches in which cells operate, particularly in multicellular organisms. In the context of various sources of biochemical "noise" individual cells face, homeostasis and phenotypic diversity in the cell population must be maintained or regulated. Adaptive mechanisms are therefore required to buffer the propagation of expression variation in networks, otherwise fluctuations in highly connected "hub" genes may drive large phenotypic changes within cells, resulting in undesirable, functionally detrimental cellular heterogeneities in the population (Eldar and Elowitz, 2010). When cells are exposed to certain environments, however, diversity within the cell population may be advantageous, in which case PoV across components in the network may be selectively harnessed to drive diversity in the cell population (Raj and van Oudenaarden, 2008; Raser and O'Shea, 2005). The immune system, for instance, is often faced with changing threats such as rapidly evolving pathogens. Thus, in some situations it may be advantageous to use a "bet-hedging" strategy whereby a range of responses are induced upon immune activation so that some cells are "pre-adapted" to unforeseen phenotypic evolutions of the pathogen.

PoV may regulate cellular heterogeneity. For example, strong PoV between two genes can render their expression tightly coupled. In this case, the number of states (as defined by the expression level of the two genes) that cells can reside in is actually less than when the genes are loosely coupled. Such a mechanism involving a negative and a positive regulator of T cell activation that are strongly coupled was found to help narrow the response diversity of naive T cells upon antigen encounter (Feinerman et al., 2008). Similar principles may apply to negative feedback or incoherent feedforward loops (Alon, 2007): restrictive PoV is helpful when feedback control is desired for maintaining expression homeostasis, while permissive PoV can result in greater expression fluctuations and thus a more phenotypically diverse cell population. In circuits involving positive feedback, the extent of PoV along the feedback could potentially be tuned to give rise to heterogeneous cell subsets with distinct phenotypes to "implement" the bet-hedging strategy discussed above.

Large-scale transcriptomic studies have highlighted differences in gene-gene correlation across disease states or subtypes using bulk materials obtained from tissues or cells (Barabasi et al., 2011; de la Fuente, 2010). The biological interpretation of these differences can be challenging, as they can reflect myriad types of variation across the sample groups, such as differences in cellular composition of the tissue and genetic background of human subjects. By contrast, our approach of assessing single cells from a single donor exposed to multiple environments helps to remove many of the potentially confounding factors and enhances our ability to generate mechanistic hypotheses, particularly at the intracellular level. For example, our results provide an intriguing hypothesis for how an environment-dependent, cytokine-mediated elevation in the rate of protein phosphorylation (or lower rate of dephosphorylation) can serve as an "amplifier" of transcript variation, which ultimately leads to more robust PoV to downstream target genes detected as elevated scGGCs in the IL-10 condition compared with CNT.

Our simulations of a circuit involving a gene (X) driving the transcription of another gene (Y) confirmed our intuition that even such a simple regulatory cascade can generate a range of PoV behavior, as different parameter combinations yielded correlations of different strengths, including many combinations that resulted in low or no correlation between the transcripts of X and Y despite their direct topological connection in the network. Incorporating the experimentally observed fold change in nuclear pATF2 levels between IL-10 and CNT conditions into our simulation confirmed that elevating the value of this parameter alone can increase scGGCs/PoV. The consistency between our simulations and experiments was robust across a range of parameter configurations and different ways of modeling the interaction between genes X and Y. However, while parameters were varied within physiologically relevant ranges estimated from the literature, some tested parameters or parameter combinations may not be realizable by cells in vivo, and our knowledge of which parameter combinations are biologically relevant remains rudimentary. In addition, while the source of variation in our model is the intrinsic stochasticity of molecular processes, considering other factors extrinsic to the X-Y system such as fluctuations in ribosome concentration may lead to alternate explanations of scGGC/dscGGC. Furthermore, the parameter space of even such a simple regulatory cascade is very large (exponential in the number of parameters), so we were not able to exhaustively test all possible model scenarios. Nonetheless, the results of our simulations under a diverse range of parameter combinations are broadly consistent with the environment-dependent PoV observed experimentally in human macrophages.

The biological consequence of selectively transmitting variation in *ATF2* expression to the ATF2 extended module genes observed in the IL-10 condition remains an interesting open question. IL-10 has been postulated to play a protective role in atherosclerosis (Han and Boisvert, 2015), a chronic inflammatory disease driven by the accumulation of cholesterol-laden macrophages in the artery wall (Moore et al., 2013). Many genes that correlated with *ATF2* under IL-10 stimulation have also been implicated in aspects of atherogenesis or lipid uptake, and we found metabolic disease- or phenotype-associated genetic variants within the active enhancers of some of these ATF2 extended module genes, which also tended to be differentially expressed in atherosclerosis plaque macrophages. While additional work will be required to explore the function of correlated single-cell expression among these genes in disease, it is tempting to speculate that it may play a role in the IL-10 mediated responses of macrophages in atherosclerosis. Since the correlations we describe arise from cell-to-cell variation and not necessarily changes in the average level of the genes as described above, traditional average level assessment of gene expression after small interfering RNA knockdown would not be a direct test of the model of PoV suggested by our data. Loss- or gain-of-function experiments coupled with single-cell analysis would also be technically difficult to interpret in this system due to large differences in transfection rates among individual cells in the population. Further complicating the interpretation of such experiments is the timing of perturbing ATF2 by knockdown or overexpression. Our current data suggest that the increased PoV in the IL-10 condition can be attributed to a higher level of phosphorylated, nuclear ATF2 without overt increases in ATF2 mRNA levels. Technically it would be challenging to specifically alter ATF2 levels or ATF2 phosphorylation concomitant with IL-10 stimulation. While it is practically more feasible to alter ATF2 levels before IL-10 stimulation, compensation mechanisms and broader consequences of altering ATF2 levels (i.e., beyond potentially affecting the module we examined) would render the results difficult to interpret in the context of the current work, which is to assess the PoV behavior concerning the specific set of genes we uncovered. New experimental techniques that disrupt PoV independent of changing average mRNA expression will be required to fully probe the function of environment-dependent dscGGCs.

IL-10 is thought to exert anti-inflammatory effects on macrophages through IL-10R-Janus Kinase (JAK)1-STAT3-mediated transcription regulation (Hutchins et al., 2013a). To the best of our knowledge, IL-10R-mediated ATF2 phosphorylation as described here has not been reported previously; however, a study utilizing STAT3 ChIP-seq in IL-10-activated macrophages suggested possible co-binding of STAT3 and AP-1 family members to DNA, and STAT3-mediated regulation of FOS expression (Hutchins et al., 2013b). While the mechanism whereby IL-10R activation leads to increased ATF2 phosphorylation in macrophages remains unknown, our results highlight how examining condition-specific PoV can help uncover potentially novel biology.

Our study has revealed that environment-dependent tuning of PoV may be a widespread mechanism that cells and cell populations harness in order to adapt to diverse environments. With the rapid increases in the quantity and quality of single-cell data, the functional impact of such adaptations is poised to be unraveled in diverse experimental systems and functional contexts.

STAR★METHODS

Detailed methods are provided in the online version of this paper and include the following:

- KEY RESOURCES TABLE
- CONTACT FOR REAGENT AND RESOURCE SHARING

- EXPERIMENTAL MODEL AND SUBJECT DETAILS
  - Human Peripheral Blood Monocyte Isolation
- METHOD DETAILS
  - Human Monocyte-Derived Macrophage Differentiation and Stimulation
  - Surface Marker Staining and Fluorescence-Activated Cell Sorting
  - Fluidigm Gene Target Selection
  - Specific Target Amplification (STA) and qPCR
  - Phospho-Flow and Immunofluorescence Staining
  - H3K27ac and ATF2 Chromatin Immunoprecipitation
  - RNA-Seq and Cap-Analysis of Gene Expression (CAGE) Library Preparation
  - Stochastic Modeling and Simulations of a Transcriptional Cascade
- QUANTIFICATION AND STATISTICAL ANALYSIS
  - Single and Ten-Cell qPCR Expression Data Preprocessing, Quality Assessment and Filtering
  - Normalization of Fluidigm Data at the Plate and Sample Levels
  - Identifying Differentially Expressed (DE) Genes
  - Application of QVARKS to Integrate Single/10-Cell Gene Expression Data
  - Computing Single- and Ten-Cell Gene-Gene Correlations (GGCs)
  - Identifying Differentially Correlated dscGGC Hubs Using a Bootstrap Procedure
  - Analysis of RNA-Seq Data
  - Mapping, Peak Calling and Differential Activity Analysis of the H3K27ac Sequencing Data
  - Mapping, Bidirectional Enhancer Finding, and Differential Activity Analysis of the CAGE Sequencing Data
  - Selection of Putative ATF2 Binding Sites and Random Control Regions for ChIP-qPCR Validation Analysis
  - Analysis Involving Disease GWAS SNP Catalog, Ingenuity, and External Microarray Data
- DATA AND SOFTWARE AVAILABILITY

SUPPLEMENTAL INFORMATION

Supplemental Information includes five figures, seven tables, and one data file and can be found with this article online at http://dx.doi.org/10.1016/j.cels.2017.03.002.

AUTHOR CONTRIBUTIONS

A.J.M., M.N., and J.S.T. designed experiments and data analysis strategies; T.P., K.P., M.N., and J.S.T. designed stochastic modeling and simulation with input from A.J.M.; T.P., K.P., and M.N. performed stochastic simulations; A.J.M., B.F., R.A.G., and C.A.-P. performed experiments; M.N., A.J.M., Y.L., W.L., and K.W. performed data analysis; A.J.M., M.N., and J.S.T. wrote the manuscript; J.S.T. guided and supervised the study.

ACKNOWLEDGMENTS

We gratefully acknowledge the assistance of Kevin Holmes and Cal Eigsti of the Flow Cytometry Section, and Owen Schwartz and Margery Smelkinson of the Biological Imaging Section, Research Technologies Branch, NIAID, NIH for single-cell sorting and confocal imaging assistance, respectively; Huizhi (Helen) Zhou and Ena Wang (Trans-NIH Center for Human Immunology and Department of Transfusion Medicine, Clinical Center, NIH) for assistance with Fluidigm gene expression analysis; Pratip Chattopadhyay (Vaccine Research Center, NIAID, NIH) for guidance with Fluidigm gene expression analysis and single-cell sorting; Emma Pierson (Stanford University) for guidance in applying ZIFA analysis; members of the Systems Genomics and Bioinformatics Unit and the Laboratory of Systems Biology for productive discussions; and Ronald Germain for critical comments on the manuscript. This work was supported by the Intramural programs of the National Institute of Allergy and Infectious Diseases and the Center for Information Technology, NIH.

Received: June 1, 2016
Revised: November 15, 2016
Accepted: March 1, 2017
Published: March 29, 2017

REFERENCES

Acar, M., Mettetal, J.T., and van Oudenaarden, A. (2008). Stochastic switching as a survival strategy in fluctuating environments. Nat. Genet. *40*, 471–475.

Alon, U. (2007). Network motifs: theory and experimental approaches. Nat. Rev. Genet. *8*, 450–461.

Altman, D.G., and Bland, J.M. (1995). Statistics notes: absence of evidence is not evidence of absence. BMJ *311*, 485.

Altschuler, S.J., and Wu, L.F. (2010). Cellular heterogeneity: do differences make a difference? Cell *141*, 559–563.

Anders, S., Pyl, P.T., and Huber, W. (2015). HTSeq – a Python framework to work with high-throughput sequencing data. Bioinformatics *31*, 166–169.

Andersson, R., Gebhard, C., Miguel-Escalada, I., Hoof, I., Bornholdt, J., Boyd, M., Chen, Y., Zhao, X., Schmidl, C., Suzuki, T., et al. (2014). An atlas of active enhancers across human cell types and tissues. Nature *507*, 455–461.

Bajikar, S.S., Fuchs, C., Roller, A., Theis, F.J., and Janes, K.A. (2014). Parameterizing cell-to-cell regulatory heterogeneities via stochastic transcriptional profiles. Proc. Natl. Acad. Sci. USA *111*, E626–E635.

Barabasi, A.L., Gulbahce, N., and Loscalzo, J. (2011). Network medicine: a network-based approach to human disease. Nat. Rev. Genet. *12*, 56–68.

Battich, N., Stoeger, T., and Pelkmans, L. (2015). Control of transcript variability in single mammalian cells. Cell *163*, 1596–1610.

Biswas, S.K., and Mantovani, A. (2012). Orchestration of metabolism by macrophages. Cell Metab. *15*, 432–437.

Blecher-Gonen, R., Barnett-Itzhaki, Z., Jaitin, D., Amann-Zalcenstein, D., Lara-Astiaso, D., and Amit, I. (2013). High-throughput chromatin immunoprecipitation for genome-wide mapping of in vivo protein-DNA interactions and epigenomic states. Nat. Protoc. *8*, 539–554.

Chang, H.H., Hemberg, M., Barahona, M., Ingber, D.E., and Huang, S. (2008). Transcriptome-wide noise controls lineage choice in mammalian progenitor cells. Nature *453*, 544–547.

Creyghton, M.P., Cheng, A.W., Welstead, G.G., Kooistra, T., Carey, B.W., Steine, E.J., Hanna, J., Lodato, M.A., Frampton, G.M., Sharp, P.A., et al. (2010). Histone H3K27ac separates active from poised enhancers and predicts developmental state. Proc. Natl. Acad. Sci. USA *107*, 21931–21936.

de la Fuente, A. (2010). From "differential expression" to "differential networking" – identification of dysfunctional regulatory networks in diseases. Trends Genet. *26*, 326–333.

Dölken, L., Ruzsics, Z., Rädle, B., Friedel, C.C., Zimmer, R., Mages, J., Hoffmann, R., Dickinson, P., Forster, T., and Ghazal, P. (2008). High-resolution gene expression profiling for simultaneous kinetic parameter analysis of RNA synthesis and decay. RNA *14*, 1959–1972.

Dunlop, M.J., Cox, R.S., 3rd, Levine, J.H., Murray, R.M., and Elowitz, M.B. (2008). Regulatory activity revealed by dynamic correlations in gene expression noise. Nat. Genet. *40*, 1493–1498.

Eldar, A., and Elowitz, M.B. (2010). Functional roles for noise in genetic circuits. Nature *467*, 167–173.

Feinerman, O., Veiga, J., Dorfman, J.R., Germain, R.N., and Altan-Bonnet, G. (2008). Variability and robustness in T cell activation from regulated heterogeneity in protein levels. Science *321*, 1081–1084.

Fieller, E.C., Hartley, H.O., and Pearson, E.S. (1957). Tests for rank correlation coefficients. I. Biometrika *44*, 470–481.

Gautier, E.L., Shay, T., Miller, J., Greter, M., Jakubzick, C., Ivanov, S., Helft, J., Chow, A., Elpek, K.G., Gordonov, S., et al. (2012). Gene-expression profiles and transcriptional regulatory pathways that underlie the identity and diversity of mouse tissue macrophages. Nat. Immunol. *13*, 1118–1128.

Gillespie, D.T. (1977). Exact stochastic simulation of coupled chemical reactions. J. Phys. Chem. *81*, 2340–2361.

Gillespie, D.T. (1992). A rigorous derivation of the chemical master equation. Physica A *188*, 404–425.

Gordon, S., and Taylor, P.R. (2005). Monocyte and macrophage heterogeneity. Nat. Rev. Immunol. *5*, 953–964.

Grün, D., Kester, L., and van Oudenaarden, A. (2014). Validation of noise models for single-cell transcriptomics. Nat. Methods *11*, 637–640.

Hamada, M., Nakamura, M., Tran, M.T., Moriguchi, T., Hong, C., Ohsumi, T., Dinh, T.T., Kusakabe, M., Hattori, M., Katsumata, T., et al. (2014). MafB promotes atherosclerosis by inhibiting foam-cell apoptosis. Nat. Commun. *5*, 3147.

Han, X., and Boisvert, W.A. (2015). Interleukin-10 protects against atherosclerosis by modulating multiple atherogenic macrophage function. Thromb. Haemost. *113*, 505–512.

Heinz, S., Benner, C., Spann, N., Bertolino, E., Lin, Y.C., Laslo, P., Cheng, J.X., Murre, C., Singh, H., and Glass, C.K. (2010). Simple combinations of lineage-determining transcription factors prime cis-regulatory elements required for macrophage and B cell identities. Mol. Cell *38*, 576–589.

Hutchins, A.P., Diez, D., and Miranda-Saavedra, D. (2013a). The IL-10/STAT3-mediated anti-inflammatory response: recent developments and future challenges. Brief. Funct. Genomics *12*, 489–498.

Hutchins, A.P., Diez, D., Takahashi, Y., Ahmad, S., Jauch, R., Tremblay, M.L., and Miranda-Saavedra, D. (2013b). Distinct transcriptional regulatory modules underlie STAT3's cell type-independent and cell type-specific functions. Nucleic Acids Res. *41*, 2155–2170.

Janes, K.A., Wang, C.C., Holmberg, K.J., Cabral, K., and Brugge, J.S. (2010). Identifying single-cell molecular programs by stochastic profiling. Nat. Methods *7*, 311–317.

Jiang, L., Schlesinger, F., Davis, C.A., Zhang, Y., Li, R., Salit, M., Gingeras, T.R., and Oliver, B. (2011). Synthetic spike-in standards for RNA-seq experiments. Genome Res. *21*, 1543–1551.

Jovanovic, M., Rooney, M.S., Mertins, P., Przybylski, D., Chevrier, N., Satija, R., Rodriguez, E.H., Fields, A.P., Schwartz, S., Raychowdhury, R., et al. (2015). Immunogenetics. Dynamic profiling of the protein life cycle in response to pathogens. Science *347*, 1259038.

Kaern, M., Elston, T.C., Blake, W.J., and Collins, J.J. (2005). Stochasticity in gene expression: from theories to phenotypes. Nat. Rev. Genet. *6*, 451–464.

Kim, D., Pertea, G., Trapnell, C., Pimentel, H., Kelley, R., and Salzberg, S.L. (2013). TopHat2: accurate alignment of transcriptomes in the presence of insertions, deletions and gene fusions. Genome Biol. *14*, R36.

Kussell, E., and Leibler, S. (2005). Phenotypic diversity, population growth, and information in fluctuating environments. Science *309*, 2075–2078.

Langmead, B., and Salzberg, S.L. (2012). Fast gapped-read alignment with Bowtie 2. Nat. Methods *9*, 357–359.

Lau, E., and Ronai, Z.A. (2012). ATF2 – at the crossroad of nuclear and cytosolic functions. J. Cell Sci. *125*, 2815–2824.

Levchenko, A., and Nemenman, I. (2014). Cellular noise and information transmission. Curr. Opin. Biotechnol. *28*, 156–164.

Liao, Y., Smyth, G.K., and Shi, W. (2014). featureCounts: an efficient general purpose program for assigning sequence reads to genomic features. Bioinformatics *30*, 923–930.

Liu, W., Ouyang, X., Yang, J., Liu, J., Li, Q., Gu, Y., Fukata, M., Lin, T., He, J.C., Abreu, M., et al. (2009). AP-1 activated by toll-like receptors regulates expression of IL-23 p19. J. Biol. Chem. *284*, 24006–24016.

Love, M.I., Huber, W., and Anders, S. (2014). Moderated estimation of fold change and dispersion for RNA-seq data with DESeq2. Genome Biol. *15*, 550.

Mariani, L., Schulz, E.G., Lexberg, M.H., Helmstetter, C., Radbruch, A., Löhning, M., and Höfer, T. (2010). Short-term memory in gene induction reveals the regulatory principle behind stochastic IL-4 expression. Mol. Syst. Biol. *6*, 359.

Martin, M. (2011). Cutadapt removes adapter sequences from high-throughput sequencing reads. EMBnet.Journal *17*, 12.

McDavid, A., Finak, G., Chattopadyay, P.K., Dominguez, M., Lamoreaux, L., Ma, S.S., Roederer, M., and Gottardo, R. (2013). Data exploration, quality control and testing in single-cell qPCR-based gene expression experiments. Bioinformatics *29*, 461–467.

Moore, W.A., and Parks, D.R. (2012). Update for the logicle data scale including operational code implementations. Cytometry A *81A*, 273–277.

Moore, K.J., Sheedy, F.J., and Fisher, E.A. (2013). Macrophages in atherosclerosis: a dynamic balance. Nat. Rev. Immunol. *13*, 709–721.

Murray, P.J. (2006). Understanding and exploiting the endogenous interleukin-10/STAT3-mediated anti-inflammatory response. Curr. Opin. Pharmacol. *6*, 379–386.

Murray, P.J., and Wynn, T.A. (2011). Protective and pathogenic functions of macrophage subsets. Nat. Rev. Immunol. *11*, 723–737.

Narayanan, M., Martins, A.J., and Tsang, J.S. (2016). Robust inference of cell-to-cell expression variations from single- and k-cell profiling. PLoS Comput. Biol. *12*, e1005016.

Novershtern, N., Subramanian, A., Lawton, L.N., Mak, R.H., Haining, W.N., McConkey, M.E., Habib, N., Yosef, N., Chang, C.Y., Shay, T., et al. (2011). Densely interconnected transcriptional circuits control cell states in human hematopoiesis. Cell *144*, 296–309.

Pedraza, J.M., and van Oudenaarden, A. (2005). Noise propagation in gene networks. Science *307*, 1965–1969.

Pham, T.H., Benner, C., Lichtinger, M., Schwarzfischer, L., Hu, Y., Andreesen, R., Chen, W., and Rehli, M. (2012). Dynamic epigenetic enhancer signatures reveal key transcription factors associated with monocytic differentiation states. Blood *119*, e161–e171.

Pierson, E., and Yau, C. (2015). ZIFA: dimensionality reduction for zero-inflated single-cell gene expression analysis. Genome Biol. *16*, 1–10.

Pina, C., Teles, J., Fugazza, C., May, G., Wang, D., Guo, Y., Soneji, S., Brown, J., Eden, P., Ohlsson, M., et al. (2015). Single-cell network analysis identifies DDIT3 as a nodal lineage regulator in hematopoiesis. Cell Rep. *11*, 1503–1510.

Quinlan, A.R., and Hall, I.M. (2010). BEDTools: a flexible suite of utilities for comparing genomic features. Bioinformatics *26*, 841–842.

Rabani, M., Levin, J.Z., Fan, L., Adiconis, X., Raychowdhury, R., Garber, M., Gnirke, A., Nusbaum, C., Hacohen, N., and Friedman, N. (2011). Metabolic labeling of RNA uncovers principles of RNA production and degradation dynamics in mammalian cells. Nat. Biotechnol. *29*, 436–442.

Raj, A., and van Oudenaarden, A. (2008). Nature, nurture, or chance: stochastic gene expression and its consequences. Cell *135*, 216–226.

Raj, A., Peskin, C.S., Tranchina, D., Vargas, D.Y., and Tyagi, S. (2006). Stochastic mRNA synthesis in mammalian cells. PLoS Biol. *4*, e309.

Raser, J.M., and O'Shea, E.K. (2005). Noise in gene expression: origins, consequences, and control. Science *309*, 2010–2013.

Rosenfeld, N., Young, J.W., Alon, U., Swain, P.S., and Elowitz, M.B. (2005). Gene regulation at the single-cell level. Science *307*, 1962–1965.

Schultze, J.L., and Schmidt, S.V. (2015). Molecular features of macrophage activation. Semin. Immunol. *27*, 416–423.

Schwanhäusser, B., Busse, D., Li, N., Dittmar, G., Schuchhardt, J., Wolf, J., Chen, W., and Selbach, M. (2011). Global quantification of mammalian gene expression control. Nature *473*, 337–342.

Shah, N., Guo, Y., Wendelsdorf, K.V., Lu, Y., Sparks, R., and Tsang, J.S. (2016). A crowdsourcing approach for reusing and meta-analyzing gene expression data. Nat. Biotech. *34*, 803–806.

Stewart-Ornstein, J., Weissman, J.S., and El-Samad, H. (2012). Cellular noise regulons underlie fluctuations in *Saccharomyces cerevisiae*. Mol. Cell *45*, 483–493.

Stojnic, R. and Diez, D.. (2015). PWMEnrich: PWM enrichment analysis. R package version 4.6.0.

Takahashi, H., Lassmann, T., Murata, M., and Carninci, P. (2012). 5' end-centered expression profiling using cap-analysis gene expression and next-generation sequencing. Nat. Protoc. *7*, 542–561.

Thattai, M., and van Oudenaarden, A. (2004). Stochastic gene expression in fluctuating environments. Genetics *167*, 523–530.

Zhang, L., and Chawla, A. (2004). Role of PPARgamma in macrophage biology and atherosclerosis. Trends Endocrinol. Metab. *15*, 500–505.

STAR★METHODS

KEY RESOURCES TABLE

REAGENT or RESOURCE	SOURCE	IDENTIFIER
Antibodies		
Human TruStain FcX (Fc receptro blocking solution)	Biolegend	Cat# 422302
Rabbit monoclonal Phospho-ATF-2 (Thr71) (11G2) Rabbit mAb (PE Conjugate)	Cell Signaling Technology	Cat# 13850
Mouse monoclonal Alexa Fluor 488 Anti-Stat3 (pY705) Clone 4/P-STAT3	BD Biosciences	Cat# 557814; RRID: AB_647098
Rat monoclonal LEAF purified anti-human IL-10R clone 3F9	Biolegend	Cat# 308806; RRID: AB_314738
Mouse monoclonal FITC anti-human CD36, clone 5-271	Biolegend	Cat# 336204; RRID: AB_1575025
Mouse monoclonal PE anti-human CD163, clone GHI/61	Biolegend	Cat# 333606; RRID: AB_1134002
Mouse monoclonal PerCP anti-CD16, clone 3G8	Biolegend	Cat# 302030; RRID: AB_940380
Mouse monoclonal PE-Cy7 anti-CD197, clone G043H7	Biolegend	Cat# 353226; RRID: AB_11126145
Mouse Monoclonal APC-Cy7 anti-CD206, clone 15-2	Biolegend	Cat# 321120; RRID: AB_2144930
Rat monoclonal Alexa Fluor 700 anti-CD195, clone HEK/1/85a	Biolegend	Cat# 313713; RRID: AB_528761
Rat monoclonal Alexa Fluor 647 anti-CD192, clone TG5/CCR2	Biolegend	Cat# 160604
Mouse monoclonal Pacific Orange anti-CD14, clone TüK4	ThermoFisher Scientific	Cat# MHCD1430; RRID: AB_10392384
Rabbit polyclonal IgG anti-human ATF-2 (C-19)	Santa Cruz Biotechnology	Cat# sc-187 (discontinued); RRID: AB_630885
Rabbit polyclonal to Histone H3 (acetyl K27) - ChIP Grade	Abcam	Cat# ab4729; RRID: AB_2118291
Chemicals, Peptides, and Recombinant Proteins		
X-vivo 15 culture media, phenol red and gentamycin free	Lonza	Cat# 04-744Q
Recombinant Human M-CSF	Peprotech	Cat# 300-25
Recombinant Human M-CSF	R&D Systems	Cat# 216-MC
Recombinant Human IFN-γ	Peprotech	Cat# 300-02
Recombinant Human TNF-α	Peprotech	Cat# 300-01A
Recombinant Human IL-4	Peprotech	Cat# 200-04
Recombinant Human IL-10	Peprotech	Cat# 200-10
disuccinimidyl glutarate	Pierce	Cat# 20593
Live/dead fixable violet stain	ThermoFisher Scientific	Cat# L34964
Critical Commercial Assays		
Dynabeads Untouched Human Monocytes negative isolation kit	ThermoFisher Scientific	Cat# 11350D
CellsDirect One-Step qRT-PCR Kit	ThermoFisher Scientific	Cat# 11753500
ChIP-IT High Sensitivity (HS) Kit	Active Motif	Cat# 53040
NEBNext ChIP-seq library prep kit	New England Biolabs	Cat# E6200
TruSeq Stranded Total RNA Library Prep Kit High Throughput	Illumina	Cat# RS-122-2203
TruSeq PE Cluster Kit v3 - cBot - HS	Illumina	Cat# PE-401-3001
TruSeq SBS Kit v3 - HS (200-cycles)	Illumina	Cat# FC-401-3001
TruSeq SR Cluster Kit v3 - cBot - HS	Illumina	Cat# GD-401-3001

(*Continued on next page*)

Continued		
REAGENT or RESOURCE	SOURCE	IDENTIFIER
NextSeq 500/550 High Output Kit v1	Illumina	Cat# FC-404-1005 (discontinued)
Deposited Data		
Sequencing and qPCR data	This study	GEO: GSE81444
Human reference genome sequences and gene/transcript annotations (UCSC hg19 assembly)	Illumina iGenomes (originally UCSC)	http://support.illumina.com/sequencing/sequencing_software/igenome.html
Experimental Models: Organisms/Strains		
Please see Table S6 for human cell donor information		
Oligonucleotides		
Please see Table S7 for oligonucleotides used in this study		
Software and Algorithms		
R		https://www.r-project.org/
Zero-inflated factor analysis (ZIFA)	Pierson and Yau, 2015	https://github.com/epierson9/ZIFA
cutadapt	Martin, 2011	https://cutadapt.readthedocs.io
Bowtie2 version 2.2.2	Langmead and Salzberg, 2012	http://bowtie-bio.sourceforge.net/bowtie2/index.shtml
Tophat2	Kim et al., 2013	https://ccb.jhu.edu/software/tophat/index.shtml
HOMER (findPeaks)	Heinz et al., 2010	http://homer.salk.edu/homer/
FANTOM5 (bidirectional enhancer calling)	Andersson et al., 2014; Takahashi et al., 2012	https://github.com/anderssonrobin/enhancers
bedtools (merge)	Quinlan and Hall, 2010	http://bedtools.readthedocs.io
PWMEnrich	Stojnic and Diez, 2015	http://bioconductor.org/packages/PWMEnrich/
htseq-count	Anders et al., 2015	http://www-huber.embl.de/HTSeq/doc/count.html
featureCounts v1.4.5-p1	Liao et al., 2014	http://subread.sourceforge.net/
DESeq2	Love et al., 2014	http://bioconductor.org/packages/DESeq2/
QVARKS	Narayanan et al., 2016	https://trackhub.niaid.nih.gov/upload/qvarks/
OMiCC	Shah et al., 2016	https://omicc.niaid.nih.gov
Fluidigm qPCR analysis software	Fluidigm	https://www.fluidigm.com/software
Leica Application Suite X	Leica Microsystems	http://www.leica-microsystems.com/products/microscope-software/software-for-life-science-research/las-x-powerful-and-flexible/
Imaris 8	Bitplane	http://www.bitplane.com/newrelease
FlowJo 9.9.3	FlowJo LLC	https://www.flowjo.com/solutions/flowjo/downloads
Other		
CAGE bidirectional enhancer locations, H3K27ac peaks/intensities	This study	UCSC Track Hub: http://genome.ucsc.edu/cgi-bin/hgTracks?db=hg19&hubUrl=https://trackhub.niaid.nih.gov/upload/macseq/hub.txt

CONTACT FOR REAGENT AND RESOURCE SHARING

Further information and requests for resources and reagents should be directed to and will be fulfilled by the Lead Contact, John S. Tsang (john.tsang@nih.gov).

EXPERIMENTAL MODEL AND SUBJECT DETAILS

Human Peripheral Blood Monocyte Isolation

Peripheral blood leukapheresis samples from de-identified, screened, healthy donors were obtained for generic research via aseptic technique under the NIH Clinical Center IRB-approved protocol 99-CC-0168 from the NIH Dept. of Transfusion Medicine (see Table S6 for donor information). Mononuclear cells were isolated using Ficoll-Paque PLUS (low endotoxin) gradient centrifugation (GE Healthcare Life Sciences). Monocytes were isolated from mononuclear cells using the Dynabeads Untouched Human Monocytes negative isolation kit (Life Technologies), which utilizes biotinylated monoclonal antibodies towards CD3, CD7, CD16a, CD16b, CD19, CD56, CD123, and CD235a, with streptavidin linked magnetic beads for depletion of non-monocyte cells. Isolated monocytes

were frozen in 10% DMSO (Sigma), 40% Human AB serum (Gemini Biosciences) and 50% X-vivo 15 media (Lonza) by the following procedure: isolated monocytes obtained using the Dynabeads isolation kit were resuspended at 20 million/mL in 4°C X-vivo 15 media (Phenol red and gentamycin free), and an equal volume of filtered, 4°C 20% DMSO/80% Human AB serum was added dropwise while mixing the cell suspension. Cells were immediately transferred to cryovials and frozen in a Nalgene Mr. Frosty cell freezing container (Thermo Scientific) in a -80 freezer for 24 hours, followed by transfer to liquid nitrogen storage. Donor information is given in Table S6.

METHOD DETAILS

Human Monocyte-Derived Macrophage Differentiation and Stimulation

Frozen monocyte vials were quickly thawed in a 37°C water bath and resuspended in X-vivo 15 media (phenol red and gentamycin free) that had been pre-equilibrated in a 37°C, 5% CO_2 incubator. Cells were plated on tissue-culture treated 6-well dishes (Corning) at 1 million cells/mL in 2 mL per well. Human macrophage-colony stimulating factor (M-CSF, Peprotech or R&D systems) was added to the media at a concentration of 100 ng/mL. On day 3 and day 6 of differentiation, all culture media was removed from the dish and replaced by fresh, 37°C, 5% CO2 incubator equilibrated X-vivo 15 containing 100 ng/mL M-CSF. Fresh media on day 6 was also supplemented with 100 ng/mL Interferon (IFN)γ and 100 ng/mL Tumor necrosis factor α (IFN+TNF treated cells), 100 ng/mL Interleukin 4 (IL-4 treated cells), 10 ng/mL IL-10 (IL-10 treated cells) (cytokines from Peprotech), or M-CSF alone (Control). Cells were harvested for analysis 24 hours after treatment by scraping in cold media.

Surface Marker Staining and Fluorescence-Activated Cell Sorting

Harvested macrophages were incubated on ice in PBS containing 5% human AB serum for 15 minutes, followed by staining for 30 minutes on ice, in the same buffer, with the following antibody cocktail: FITC anti-CD36, clone 5-271 (Biolegend); PE anti-CD163, clone GHI/61 (Biolegend); PerCP anti-CD16, clone 3G8 (Biolegend); PE-Cy7 anti-CD197, clone G043H7 (Biolegend); APC-Cy7 anti-CD206, clone 15-2 (Biolegend); Alexa Fluor 700 anti-CD195, clone HEK/1/85a (Biolegend); Alexa Fluor 647 anti-CD192, clone TG5/CCR2 (Biolegend); Pacific Orange anti-CD14, clone TüK4 (Life Technologies). Following staining, cells were washed once with ice cold PBS, and resuspended in ice cold PBS containing a 1 in 1000 dilution of Pacific Blue Fixable Live/Dead stain (Life Technologies), which is a fluorescent dye reactive with cellular amines. When the cell membrane becomes permeable, the dye gains access to intracellular amines and hence the fluorescence of the cell increases. For sorting, cells were gated upon Forward scatter (FSC)-width versus side scatter (SSC)-area for doublet discrimination, followed by gating on Pacific blue low (membrane intact) cells (versus FSC-area). A 100 μm nozzle was used at 20 PSI pressure and a drop drive frequency of 34.5 kHz. Sorting was performed on a FACSAriaII (Becton Dickinson) and FACSDiva version 6.1.3 software using Single cell precision mode with default parameters (Yield mask = 0, Purity mask = 32, Phase mask = 16). Sorting was done using index mode to retain information on fluorescence measurements of protein marker expression for each sorted cell. Sort alignment was checked immediately before sorting, by sorting beads onto a covered PCR plate and confirming that the droplets land in the center of several different wells across the plate. Cells were deposited into individual wells of a low-profile 96 well PCR plate (Bio-rad) containing 2.5 uL CellsDirect 2x Reaction Mix (Life Technologies), 0.05 uL Ambion SUPERase-In RNAse inhibitor (Life technologies), and 1 uL RNAse-free water. Cells from different treatment groups were sorted into alternating wells across the plate, to avoid positional or "edge" effects across the plate (Figure 2A). Each plate contained a "no template" control well, and a seven point dilution of a pooled RNA sample derived from a combination of RNA isolated from non-treated, IFNγ, lipopolysaccharide (LPS), IFNγ + LPS, or IL-4 -treated macrophages, as a reference positive control. Control RNA was isolated using the miRNeasy mini kit (Qiagen). All wells except the positive control wells also contained ERCC RNA reference standards (Life Technologies) spiked in at 1/50,000 final dilution from the stock ERCC mixture. Because cell lysis occurs immediately after sorting into the PCR buffer and the PCR plates are not amenable to microscopy, sorted cells cannot be visualized in the same wells used for qPCR analysis; instead, single cell deposition was confirmed by sorting Hoescht-stained macrophages into 96 well culture plates containing 50 uL of X-vivo 15 media using the same sorting parameters as used during sorting into the PCR plates and observed under epifluorescence microscopy. Although single cells can be difficult to visualize in the large volume of the culture plate, individual cells could be found in a fraction of the wells, and no evidence of doublets was found. Cell deposition in wells of the PCR plate had a high success rate, with only 1-2% of wells on the PCR plates negative for amplification by qPCR. After sorting, plates were sealed with foil film (Bio-rad) and centrifuged at 2000x G for 3 minutes and frozen at -80°C.

Fluidigm Gene Target Selection

To select the 96 genes to be measured by qPCR using primer/probe assays (Life Technologies or IDT) that might be informative of cellular heterogeneity and responses, several approaches were used: 1) literature based, selecting for genes relevant to macrophage activation responses; 2) selecting for the most variable genes across a compendium of human macrophage-related microarray experiments deposited in the Gene Expression Omnibus; 3) a selection of module-representative genes from gene expression modules derived from microarray mRNA expression measurements across diverse human immune cell types, from (Novershtern et al., 2011); 4) transcription factor "cascades", containing genes with known regulatory relationships (see also Figure 2B). Genes from core cellular or metabolic processes were also selected, including lipid and cholesterol biosynthesis and processing. Genes in common across more than one of these selection sources were chosen whenever possible. qPCR assays targeting these genes were tested with iterative rounds of quality control to check for assay linearity and sensitivity to detect expression at the single cell level. Assays

failing quality control were replaced with new assays targeting the same gene or with assays targeting different genes identified from the selection strategies but not tested in earlier rounds. See Table S7 for a list of primer/probe assays used in this study.

Specific Target Amplification (STA) and qPCR

Sort plates containing single/ten cell sample RNA were thawed, and 1.35 uL of STA mix (1.25 uL of a pool of 96 Taqman assays at 0.2x concentration, and 0.1 uL Superscript III/Platinum Taq mix (CellsDirect kit, Life Technologies)) were added to each well. Plates were then sealed with clear film (Bio-rad) and centrifuged at 2000x G for 3 minutes and STA was run on a CFX Connect thermal cycler (Bio-rad) with the following cycling parameters: 50°C for 15 mins, 95°C for 2 minutes, then 18 cycles of 95°C for 15 seconds and 60°C for 4 minutes. Plates were then placed on ice and cold 10 mM Tris pH 8.0, 0.1 mM EDTA buffer was added to each well at 20 uL per well. Samples were then analyzed by qPCR on the Fluidigm Biomark instrument using 96.96 chips according to manufacturer's instructions (Fluidigm). Briefly, 2.25 uL per well of each amplified, diluted single cell sample was mixed with 2.5 uL Ssofast 2X Probes Supermix (Bio-rad) that had 0.5X ROX reference dye added (from the CellsDirect Kit, Life Technologies), and 0.25 uL sample loading reagent (Fluidigm). Taqman assays (20x concentration) were combined 1:1 with Assay loading reagent (Fluidigm). Sample and assay mixes were then added to the wells of the 96.96 chip for gene expression measurement. The normal speed cycling gene expression protocol was used, with 40 cycles of amplification. Data were exported from Fluidigm Real-time PCR Analysis software version 3.1.3, using Linear (Derivative) Baseline method, a global threshold of 0.01, and a 0.65 quality threshold, parameters which were found to exclude non-specific amplification and reduce plate-plate variation. Three Fluidigm qPCR experiments were performed: the discovery experiment referred to as Exp.1 or Jul9, and two validation experiments (Exp. 2 (Jul23) and Exp. 3 (Dec. 13)).

Phospho-Flow and Immunofluorescence Staining

For the intracellular staining of phosphorylated ATF2 and STAT3 for flow cytometry analysis (phospho-flow), macrophages were cultured and treated as above, and fixed at the indicated time points using formaldehyde added directly to the culture media to a final concentration of 1.6%. After 10 minutes of incubation in fixative, cells were harvested by scraping and washed once by centrifugation (300 x G, 5 minutes) and resuspension with PBS with 1% fetal calf serum and 2 mM EDTA (hereafter referred to as staining buffer). Cells were resuspended in 100% ice cold methanol and incubated at -20°C overnight. After adding an 2x volume of staining buffer and centrifugation, cells were then resuspended in staining buffer containing Human Trustain FcX (Biolegend) to block non-specific antibody binding, and stained for 1hr at room temperature using anti-phosphorylated Thr71 ATF2 (Cell Signaling Technology, clone 11G2) and anti-phosphorylated Tyr 705 STAT3 (BD Biosciences, clone 4/P-STAT3). Following 2 washes in staining buffer, cells were analyzed on a BD LSR Fortessa (BD Biosciences). For some experiments, cells were pre-blocked for 1 hour with anti-IL10R antibody (Biolegend, clone 3F9, low-endotoxin azide-free) at 30 μg/mL. Total ATF2 protein was stained in fixed and permeabilzed cells (FoxP3 staining kit, eBioscience) using a rabbit polyclonal antibody (ab131484, Abcam), followed by staining with a fluorescently labeled secondary prior to flow cytometry analysis.

For analysis via confocal imaging, cell plated on coverglass chamber slides (Nunc Lab-Tek, Thermo Scientific) were fixed in formaldehyde as above, washed in PBS three times, then permeabilized in 100% methanol for 10 minutes at -20°C, with 2 further PBS rinses. Following blocking as above, cells were stained with the same PE-conjugated anti-pATF2 and the nuclei were stained with DAPI. Following washing in PBS, the cells were imaged in PBS using a confocal microscope equipped with Leica HyD PMT detectors (Leica Microsystems). pATF2 staining in the nucleus was quantified in the 3D stack images using Imaris (Bitplane Software).

To examine the relationship between ATF2 and STAT3 phosphorylation as measured by phospho-flow staining (Figure S4D) and account for the possibility that cell size differences may drive spurious correlation between pATF2 and pSTAT3 signals, we fit the following linear model in R notation: pSTAT3 ~ FSC + SSC + pATF2, and correct the pSTAT3 signal of each cell by subtracting the cell size surrogate values (FSC and SSC area), multiplied by their estimated model coefficients. The resulting pSTAT3 residuals were used to compare the median size-corrected pSTAT3 signal of high and low pATF2 expressing fractions of cells; a non-zero difference for the treated cells indicates a correlation between pSTAT3 and pATF2 levels. To test this correlation statistically, an interaction model was fitted using the R "lm" function (R notation: pSTAT3 ~ pATF2 + Condition + pATF2:Condition + FSC + SSC, where condition is CNT (baseline), IL-10 2 hr, or IL-10 24 hr), then the slope and p value of the interaction term pATF2:Condition was checked.

H3K27ac and ATF2 Chromatin Immunoprecipitation

To examine enhancer-associated H3K27 histone acetylation in IL-10 vs. CNT, 10 million macrophages per sample were cultured in 10 cm culture dishes, treated with or without IL-10 (10 ng/mL) for 24 hours. Following treatment incubation, plates were rinsed once with room temperature PBS, and fixed using 1% formaldehyde for 10 minutes on an orbital shaking platform set to slowly mix the fluid. The fixation reaction was then quenched by adding glycine to a final concentration of 0.15 M and incubating a further 5 minutes. Plates were then rinsed 1x with ice-cold PBS containing protease inhibitors and cells were harvested from the plates by scraping. Cells were centrifuged in 15 mL conical tubes 5 minutes at 300 x G at 4°C. Immunoprecipitation was carried out as following the method of Blecher-Gonen (Blecher-Gonen et al., 2013), with the following modifications: sonication was performed using a Covaris S2 instrument in 1 mL tubes, 20 million cells per tube, intensity 5, duty cycle 20%, 200 cycles per burst for 6 minutes; 75 μl Protein G microbeads (Invitrogen) and 3 ug of H3K27ac antibody (Abcam ab 4729) were used. Illumina sequencing libraries were prepared using the NEBNext ChIP-seq library prep kit (NEB) and sequenced on a Illumina HiSeq 2000 (see Table S6 for sequencing information).

To detect ATF2 chromatin binding to specific regions via ChIP-seq and qPCR, we fixed the cells as above, except cells were incubated with 2 mM disuccinimidyl glutarate (Pierce Cat # 20593) in PBS for 20 minutes prior to formaldehyde fixation, and nuclei were isolated as in the protocol given by (Blecher-Gonen et al., 2013). 200uL of chromatin was then placed in 0.65 mL eppendorf tubes and sonicated using the Bioruptor Pico (Diagenode) on High for 16 cycles of 30 seconds on and 30 seconds off. Immunoprecipitation was performed using an anti-ATF2 c-terminus antibody (sc-187, Santa Cruz Biotechnology) and the High sensitivity ChIP kit (Active Motif). ChIP-seq libraries were prepared as was done for H3K27ac libraries above, or detection of specific target regions was performed using qPCR on the Biomark HD (Fluidigm) using Fluidigm's protocol for Evagreen assays with 21 cycles of preamplification (1x concentration of each primer; ABI Taqman Preamp master mix (Life Technologies)) prior to Fluidigm qPCR. Assays used for ChIP-qPCR were from IDT. Please see Table S7 for list of primers used in this study.

RNA-Seq and Cap-Analysis of Gene Expression (CAGE) Library Preparation

RNA-seq data were utilized from an independent study of bulk-level macrophage activation (our unpublished data). 18 hrs post-treatment, cells were harvested from IL-10 and CNT macrophages cultured in 48 well dishes by the direct addition of Trizol to the cells after media removal, and RNA-seq was isolated using Zymo Direct-zol spin columns. RNA-seq libraries were prepared using the Illumina Truseq Ribo-Zero kit with 100-500 ng total starting RNA.

CAGE libraries were made following the method of Takahashi *et al.* (Takahashi et al., 2012). Briefly, 1-5 ug of RNA is reverse transcribed, followed by chemical biotinylation of the 5′ cap. Following selection of capped RNA:cDNA hybrids, linkers are ligated that allow second strand cDNA synthesis and provides a recognition site (in conjunction with the site included in the RT primer) for the EcoP15I restriction enzyme, which is used to cleave the fragments 27 nucleotide downstream of the recognition site. Following further processing, these 27 nucleotide "CAGE tags" are then sequenced, and represent the 5′ ends of the RNA, including enhancer RNAs.

Stochastic Modeling and Simulations of a Transcriptional Cascade

We simulated a stochastic model of a transcription network that consists of two genes connected by a single edge X → Y (Figure S1A). In this model, the promoters of both genes undergo stochastic transitions between the "ON" state in which transcription can occur and the "OFF" state in which transcription is not possible. The model incorporates the basic biochemistry of transcription and degradation, including parameters such as the rate of mRNA degradation and translation. Similar models have been previously used to study stochasticity in gene expression (Kaern et al., 2005; Mariani et al., 2010; Raj et al., 2006). In addition, provided that the promoter of gene Y is in the "ON" state, the transcription of gene Y is regulated by the protein product of gene X. We also considered augmented versions of this model to capture the activation of protein X via post-translational modification (phosphorylation) and subsequent nuclear translocation (Figure 5B). We calculated the Spearman correlation coefficient between the mRNA copies of X and Y at a fixed time point for each of the parameter configurations we simulated.

In detail, the dynamics of the X system is specified by the following reaction scheme:

$$g_X \underset{k^X_{off}}{\overset{k^X_{on}}{\rightleftharpoons}} g^*_X \tag{1}$$

$$g^*_X \xrightarrow{k^X_m} g^*_X + m_X\ , \tag{2}$$

$$m_X \xrightarrow{k^X_p} m_X + p_X\ , \tag{3}$$

$$m_X \xrightarrow{\delta^X_m} \phi\ , \tag{4}$$

$$p_X \xrightarrow{\delta^X_p} \phi\ . \tag{5}$$

Here, g_X, g^*_X, m_X, p_X refer to the inactive and active gene (i.e., whether transcription can be initiated or not), the mRNA and the gene product, respectively. Furthermore, κ^X_{on}, κ^X_{off} denote the promoter activation and inactivation rate (only in the "ON" state can transcription occur), whereas k^X_m, k^X_p are the rates of transcription and translation, respectively, and δ^X_m, δ^X_p are the corresponding rates of mRNA and protein degradation, respectively.

Similar to gene *X*, gene *Y* can also switch stochastically between the ON and OFF states. In addition, however, provided that gene Y is in its active state, its expression is regulated by the protein product of *X*, i.e. the protein p_X acts as an activator of gene *Y* by binding to the Y promoter. Neither auto-regulation nor feedback was assumed. The transcription rate of Y is described by a Hill function:

$$k^Y_m \frac{p^n_X}{p^n_X + K^n}\ , \tag{6}$$

where k_m^Y, K, n denote the maximal transcription rate, the activation coefficient (set to 133.333 in all simulations), and the Hill coefficient (set to 1 in all simulations), respectively. Everything taken together, the Y system is described by the reaction scheme:

$$g_Y \underset{\kappa_{off}^Y}{\overset{\kappa_{on}^Y}{\rightleftharpoons}} g_Y^* , \tag{7}$$

$$g_Y^* \overset{k_m^Y \frac{p_X^n}{p_X^n + K^n}}{\rightarrow} g_Y^* + m_Y , \tag{8}$$

$$m_Y \overset{\delta_m^Y}{\rightarrow} \phi \tag{9}$$

The choice of the two-gene network model parameter values was based on experimentally estimated rate constants as well as mRNA and protein half-lives previously reported in the literature (see Table S1) (Dölken et al., 2008; Jovanovic et al., 2015; Mariani et al., 2010; Rabani et al., 2011; Raj et al., 2006; Schwanhäusser et al., 2011). However, absolute values of rates and half-lives are typically difficult to quantify. For example, considerably discordant values, for instance, for mRNA half-lives have been obtained (Rabani et al., 2011; Schwanhäusser et al., 2011). It is generally not clear whether the observed discrepancies reflect genuine biological differences among the cell lines used or they were a result of differences in and/or due to limitations of experimental protocols, data analysis methods, and computational models. Furthermore, the measured parameter values were obtained from cell populations and thus single cell measurements could differ (Rabani et al., 2011; Schwanhäusser et al., 2011). In this context, it is worth noting that different absolute values have been reported for the same cell line (Dölken et al., 2008; Schwanhäusser et al., 2011).

We conducted simulations using Gillespie's Direct method (Gillespie, 1977, 1992) implemented in C++ across the full range of parameter configurations as follows: We divided each parameter range into 10 grids with equal intervals in original scales (κ_{on}^x, κ_{off}^x, κ_{on}^y, κ_{off}^y) or logarithmic scales ($k_m^x, \delta_m^x, k_p^x, \delta_p^x, k_m^y, \delta_m^y$). Of 10^{10} possible parameter combinations, we sampled 10^5 parameter configurations by randomly selecting a single value out of 10 possible values for each parameter. The number 10^5 was determined based on practical run time considerations on a high-performance computation cluster. By sampling a large number of parameter combinations, we can explore the phase space of correlations between X and Y mRNAs comprehensively.

For each randomly selected parameter configuration, we ran 500 realizations (or cells) starting from $m_x = m_y = p_x = p_y = 0$, and with both gene X and gene Y in off states. Then snapshots of the system at 72 hours were taken. We applied one filtering procedure based on biological relevance right before conducting the simulation. By assessing the asymptotic behaviors of the ODEs describing the system deterministically, we can obtain stationary mean copy numbers for mRNAs and proteins. If these estimated values exceed biologically meaningful ranges (for mRNA 1000 copies, for protein 2 million copies), we do not simulate that parameter combination. We then generated the histogram of Spearman correlation strengths for the remaining parameter combinations.

The modeling and simulation scheme described thus far was used in Figure S1 to confirm our conceptual intuitions about how different biochemical parameters related to expression of and interaction between X and Y influence the correlation strength between their mRNA transcripts across simulated cells. We also augmented this model (Figure 5) to capture the activation of a protein via post-translational modification (phosphorylation) and subsequent nuclear translocation as in the case of ATF2, by adding the following activation/deactivation and related reactions for protein X, and making only the activated form AP_X instead of p_X affect the transcription of gene Y through the Hill's function (by replacing the p_X in reaction scheme (6) or (8) by AP_X in reaction (12)).

$$p_X \underset{\kappa_{poff}^X}{\overset{\kappa_{pon}^X}{\rightleftharpoons}} AP_X \tag{10}$$

$$AP_X \overset{\delta_p^X}{\rightarrow} \phi \tag{11}$$

$$g_Y^* \overset{k_m^Y \frac{AP_X^n}{AP_X^n + K^n}}{\rightarrow} g_Y^* + m_Y \tag{12}$$

We explored the parameter space of this augmented model under two schemes, with stochastic simulations performed and correlation strength between mRNAs X and Y calculated for each parameter configuration thus explored.

- In a *random-scan* scheme (Figure S5D), we started with the randomly selected configurations described above that also exhibited high correlation in the original model (the 622 configurations with scGGC > 0.7 in Figure S1C). For each such configuration, we used the rate constant values defined by the configuration, and set the new parameters k_{poff}^X at 0.0001 events/hr/molecule, and k_{pon}^X at 1 events/hr/molecule for the High-AP_X simulated environment and a value less than 1 for the Medium(Med)-AP_X simulated environment that is chosen so as to target a 1.74 fold increase of average AP_X in High-AP_X relative to Med-AP_X environment (similar to experimental observations). Since the steady-state dynamics of our models are difficult to characterize exactly using deterministic ODE asymptotics, this targeted 1.74 fold increase was actually

realized in our simulations for only a subset of the 622 high-correlation parameter configurations, and the remaining configurations were ignored for further analysis. Specifically, 430, 421 or 435 parameter configurations realized an average AP_X fold increase of 1.74 ± 10% among simulated cells at 72 hours in High-AP_X relative to Med-AP_X environment for the 0%, 50% or 100% boxplots shown in Figure S5D, respectively.

- In a *targeted-scan* scheme (Figure 5), we performed a more targeted search of the parameter space by choosing different values of κ^Y_{on} and κ^Y_{off} from a grid of 10 x 10 data points within their range (to assess if the role of Y enhancer/promoter accessibility in influencing correlations is consistent with our experimental results), while keeping the remaining rate constants fixed at values shown in Figure 5C (to achieve a high continuous-type correlation between X and Y mRNAs). Spearman correlation values were calculated for the different parameter configurations at a fixed "snapshot" time point of 504 hours, instead of 72 hours as before to reflect changes in steady-state behavior of the new models. Again each explored configuration was simulated under both High-AP_X and Med-AP_X conditions as in the random-scan scheme using k^X_{poff} value of 0.0001 events/hr/molecule and k^X_{pon} values of 1 or 0.5367 events/hr/molecule respectively so as to achieve the same fold change of 1.74 in average AP_X level between the two conditions.

We also tried alternate setups of this augmented model (Figure S5) to capture settings where the activated form of protein X not only influences the transcription of gene Y through Hill's function as above, but also dynamically affects accessibility of the Y promoter/enhancer. We modeled this by having κ^Y_{on} depend partly on the level of activated protein AP_X through the same Hill's function ($AP^n_X/(AP^n_X + K^n)$ abbreviated below by the function $Hill(AP_X)$), with the relative contribution of AP_X vs. other general chromatin regulation factors in influencing κ^Y_{on} set using an extra parameter *frac* ranging from 0 to 1.

$$\kappa^Y_{on(alternate)} = \kappa^Y_{on_{(specified)}} * (1 - frac) + \frac{\kappa^Y_{on_{(specified)}}}{Hill(averageAP_X)} * frac * Hill(AP_X)$$

The AP_X-influence fraction (*frac*) of 0% on κ^Y_{on} corresponds to the augmented model described above where κ^Y_{on} is held constant across the whole simulation. For non-zero AP_X-influence fractions of 50% or 100% for instance, the scaling of the second term by $Hill(averageAP_X)$ maintains the average fraction of simulated cells with accessible Y promoter/enhancer to be the same across different values of *frac* (to an approximate extent since we approximate average($Hill(AP_X)$) by $Hill(averageAP_X)$). In other words, the scaling helps maintain the average $\kappa^Y_{on(alternate)}$ rate at the same value of $\kappa^Y_{on_{(specified)}}$ across different values of *frac*, and makes it easy to compare and visualize results from these models. Note that in these discussions, *average* means the average across all simulated cells in the fixed steady-state or snapshot time point (which allows for instance the approximation of $averageAP_X$ using deterministic ODE asymptotics and other assumptions as $\frac{\kappa^X_{on}}{\kappa^X_{on}+\kappa^X_{off}} \frac{k^X_m}{\delta^X_m} \frac{k^X_p}{\delta^X_p} \frac{k^X_{pon}}{k^X_{pon}+k^X_{poff}+\delta^X_p}$; this expression is also used to determine the k^X_{pon} value for the High-AP_X and Med-AP_X environments given specific values of all other parameters).

QUANTIFICATION AND STATISTICAL ANALYSIS

Please note that statistical tests used are listed with the corresponding p values in the text and figure legends. Unless otherwise specified, boxplots in figures show the median as a line inside the box and the first and third quartiles as the lower and upper box edges (hinges), with whiskers extending from the hinge to the last point within 1.5x the inter-quartile range of the hinge and outlier points indicating data beyond the whiskers.

Single and Ten-Cell qPCR Expression Data Preprocessing, Quality Assessment and Filtering

We convert gene expression data exported from Fluidigm Real-time PCR Analysis software from Ct (Cycle threshold) units to the more convenient Et=40-Ct units, as in previous studies (McDavid et al., 2013). Under standard qPCR assumptions, the Et value of a gene measured in a sample is directly proportional to the logarithm of the mRNA abundance of the gene in the sample, after subtracting a constant term corresponding to the Et of a minimum detectable quantity of the gene's mRNA (McDavid et al., 2013). The standard curves based on a dilution-series experiment support this proportional relationship for gene assays in our panel (the standard curves for all but four of the 96 gene assays in our panel exhibit R^2 at least 0.8 and slope at least -3.32, with -3.32 corresponding to qPCR efficiency of 100%). Note that we discarded gene assays with poor standard curve behaviors in earlier rounds of gene panel selection as described above. The dilution-series experiment was done using a standard mRNA mixture that was added to each sort plate as described above. A total of seven dilutions were performed spanning more than a 10,000-fold range of medium to high mRNA concentrations, and each dilution had eight technical replicates (spread one per plate across the eight Fluidigm qPCR plates of our discovery experiment, except for one dilution which had only seven replicates due to an outlying measurement).

We assign samples where a gene is not detected an Et of –Infinity, and call them as non-detected samples or non-detects of the gene (detects of the gene are the remaining samples). We exclude samples with fewer than 10% of all assayed genes detected from downstream analysis, as they may reflect wells that did not have sorted cells. The number of such missing samples in a single Fluidigm plate can be used as a quality metric – 10 of the total 16 plates in our discovery/validation experiments had no missing samples and the rest had 3 or fewer missing samples per plate. Before performing any correlation analysis, we also removed outliers among the detects of a gene within each treatment condition, in order to guard against technical noise and stochastic detects at very low levels of expression. We chose these outliers for a gene in a condition as the detects whose across-plate normalized

Et values as described next are 3 MAD (median absolute deviation) units away from the median (note that most outliers were below the median, a pattern consistent with increased technical noise at very low levels of expression). Of all the four conditions, data from two of them (CNT and IFN+TNF) were also used in the QVARKS manuscript for a different purpose (development and testing of a Bayesian method for inferring cell-to-cell variation from simultaneous single/10-cell data; see (Narayanan et al., 2016) and description of QVARKS below).

To visualize single and ten-cell qPCR data in reduced dimensions, zero-inflated factor analysis was used (Pierson and Yau, 2015).

For each gene pair shown in Figure 3A, the 2D ten-cell density is simulated for the gene pair using 1000 random 10-cell aggregates computed from the single-cell data, and each gene's simulated values are shifted separately by a single normalization factor to align the average gene expression of the simulated and observed 10-cell data.

Normalization of Fluidigm Data at the Plate and Sample Levels

To profile a large number of cells, we uniformly distributed single cells and 10-cell pools from the different treatment groups across multiple Fluidigm plates (e.g., 8 plates in the discovery experiment), all of which could not be run in one batch on the same day. To track and correct potential batch/plate effects, we spiked-in ERCC transcripts (Jiang et al., 2011) to each sample, and normalized all gene measurements using the plate median of the ERCC control mRNA with the highest Et value (ERCC-0003). In detail, we shifted all detected gene measurements in a plate by a plate-specific global factor, which is chosen such that the median ERCC-0003 level of the shifted data across all (non-dilution-series) samples in the plate becomes the same across all plates. After removing plate effects using this plate-level normalization, data from different plates are concatenated to obtain one single/10-cell dataset per experiment.

For gene-gene correlation analyses across samples, we also did subsequent sample-level normalization by utilizing the variation of control mRNA levels across samples within/across plates. This sample-to-sample variation in ERCC levels correlated with that of highly expressed genes (Narayanan et al., 2016), suggesting well-to-well differences in the starting amount of mRNA or other such technical factors were at play in addition to independent measurement errors. To correct for this potential technical variation, we fitted a linear regression model (expressed in the notation of statistical environment R as "*Gene-expression* ~ *Plate* + *ERCC-0002-expression* + *ERCC-0003-expression* + *ERCC-0044-expression*") separately in each condition, and took the fitted residuals as the normalized log-expression of the gene (log-expression is simply referred to as expression in the text when it is clear from the context). Note that this regression model, which allows plate effects to be different for different genes, is fitted to the plate-level normalized data discussed above where the same plate effect was assumed for all genes.

Differences in size among cells are known as a strong "extrinsic" factor that can influence the mRNA abundance of many genes and can thus be a key driver of scGGCs in a cell population (Battich et al., 2015; Eldar and Elowitz, 2010). To assess the effect of cell size, we adjusted 10-cell expression data using flow-cytometric surrogate measures of cell size. This analysis indicated that gene-gene correlations were highly concordant before and after cell-size adjustment of the 10-cell data (Figure S3C); thus, the significant scGGCs we observed were unlikely to be driven by cell size differences. To account for cell-size differences, we simply add to the regression model above the variables Forward Scatter Area (FSC-A) and Viability stain as surrogate measures of cell size (note that sorted cells are from the viable gate only, but all cell surface proteins will be stained by the viability dye in live cells). The residuals from this regression model is used in an analysis to compute the cell-size-corrected 10-cell based gene-gene correlations. Note that the FSC-A value of a 10-cell sample is taken as the sum of the per-cell FSC-A values of the 10 cells in the sample obtained from the index-sorted flow cytometry data. The Viability of a 10-cell sample is calculated similarly but after accounting for the logicle transform (Moore and Parks, 2012)– specifically it is taken as the logicle transform of the sum of the untransformed ("unlogicled") per-cell Viability values of the 10 cells in the sample. For this analysis, the per-cell flow cytometry data in the form of raw fluorescence intensities (FCS files) were imported into FlowJo (v9.6) for compensation, a procedure that corrects biases caused by spectral overlaps, and the corrected intensities were exported so that we could transform them further using the statistical software R. We specifically applied the logicle transform with default parameters shown below to handle the large dynamic range of fluorescence intensities. This transform is similar to the log transformation but better suited to the representation of flow cytometry data especially when the signal is low (Moore and Parks, 2012).

$$\text{logicle}(X) = \begin{cases} T * 10^{-(M-W)}\left(10^{X-W} - p^2 * 10^{-\frac{X-W}{p}} + p^2 - 1\right), & X \geq W \\ -T * 10^{-(M-W)}\left(10^{W-X} - p^2 * 10^{-\frac{W-X}{p}} + p^2 - 1\right), & X < W \end{cases}$$

where $T = 262144$, $M = 4.5$, $W = 0.5$, and p is the solution to the equation $2p\ (\log p)/(p+1) = W$.

Identifying Differentially Expressed (DE) Genes

DE genes are detected from single-cell data using the Wilcoxon test to increases robustness against non-detects in single-cell data, and from ten-cell data using a linear model described below. Note that since individual single- or 10-cell samples come from a single biological replicate (donor), the resulting DE p value and FDR estimates (Table S3A/B) can be over-optimistic – so we also used RNA-seq data from multiple biological replicates (donors) to assess DE (Figures S3G and S5A). The linear regression model used to detect DE genes from 10-cell data models each gene's 10-cell measurement across all treatments against the predictor variables: *Treatment* to model fold change in each treatment vs. CNT, *ERCC expression* to adjust for potential well effects, and *Plate* variable to

adjust for potential plate effects. Non-detects are assumed to have zero expression (0 Et). In R notation, the linear model is "*10-cell expression of a given gene ~ Treatment + ERCC-0002-expression + ERCC-0003-expression + ERCC-0044-expression + Plate*". We extract the DE p values from the fitted model as the significance of the treatment coefficients (log fold change of treatment vs. CNT) being different from zero, adjust them for multiple testing using the Benjamini-Hochberg procedure separately for the IL-10 vs. CNT, IL-4 vs. CNT and IFN+TNF vs. CNT pairwise comparisons, and declare genes at adjusted $P < 0.1$ as DE hits. In addition, the same process is repeated for the two validation experiments, and only genes that come up as DE hits in the discovery and the two validation experiments in the same direction (up-regulation in all three experiments, or down-regulation in all three) are reported as final DE hits in Table S3B.

Application of QVARKS to Integrate Single/10-Cell Gene Expression Data

QVARKS (Quantify VARiation from K- and Single- cells) is a model-based Bayesian approach we developed (Narayanan et al., 2016) to combine information from single-cell and 10-cell data simultaneously to reliably infer the parameterized distribution of a gene's expression across individual cells. QVARKS model takes into account that a non-detected single/10-cell sample in a qPCR gene assay could indicate either zero transcripts of the gene in the sample or non-zero transcripts that missed detection for technical reasons – distinguishing these two scenarios is a key challenge in single-cell measurements and utilizing simultaneously obtained 10-cell measurements with enhanced sensitivity can help address this challenge. We applied QVARKS separately to each gene-condition combination using default MCMC (Markov Chain Monte Carlo) settings and default model assessment criteria (for deciding which gene-condition combinations are successfully modeled). To generate the heatmaps of discrete (ON vs. OFF cells) or continuous (variance among ON cells) heterogeneity in Figures S2F and S2G, we excluded inferred parameters whose posterior distributions had large variances (specifically posterior CV greater than 50% for any of the three single-cell gene expression distribution parameters: namely 1) the fraction of ON vs. OFF cells, and 2) the mean and 3) variance among ON cells).

Computing Single- and Ten-Cell Gene-Gene Correlations (GGCs)

We used the Spearman correlation coefficient to quantify continuous correlation between two genes (a rank-based metric that helps guard against outliers), and log odds ratio to measure discrete correlation (a contingency table-based metric that has a desirable feature of not being skewed by the marginal distribution of the two variables, and computed using the R *vcd* package, which adds 0.5 to all table entries as a smoothing factor if any table entry is empty). We first computed both types of correlations in single-cell data, and then verified that both were significantly concordant with the continuous correlations found using the 10-cell data. We corrected for multiple testing separately within each condition using the Benjamini-Hochberg FDR procedure, and retained only correlations found at FDR 20% in each condition to assemble the gene-gene correlation network in Figure 3. To reduce the burden of multiple testing, we only considered gene pairs with sufficient data. Specifically within each condition, we tested continuous correlations only among genes with detection rates of at least 80% in 10-cell data and 50% in single-cell data, and discrete correlations only among genes with Shannon entropy of at least 0.7 in single-cell data. As described above, the continuous correlations were computed using the plate- and sample-level normalized data to exclude correlations driven by well-to-well variations in spiked-in control mRNA levels, which likely reflect technical variation (Narayanan et al., 2016). Discovery and validation experiments utilized independent cell culture, sorting, and Fluidigm gene-expression analysis of cells derived from a single donor, with experiments one and two taking place two weeks apart, and experiment three taking place 5 months later.

Identifying Differentially Correlated dscGGC Hubs Using a Bootstrap Procedure

We use a bootstrap procedure to test whether a set of gene-gene correlations (reflecting the linkage of one "hub" gene to several other "partner" or "module" genes) in one condition is significantly different in their correlation strengths when compared to another condition. Note that a simple procedure that selects gene-gene links in one condition's scGGC network that is absent in another condition's scGGC network (e.g., using Figure 3) could point to potential dscGGC hub genes, but a statistical test is required to assess significance, thereby avoiding any misleading dscGGC signals that arise from the specific FDR cutoff used to reconstruct each condition's network (for instance, a strict FDR cutoff could exclude certain marginally correlated gene pairs from a network (Altman and Bland, 1995)).

To derive an aggregate strength of the change in a set of hub-gene correlations between two conditions (hub dscGGC effect size), we estimate the strength of the change in the correlation of each hub-gene pair (hub-gene dscGGC effect size) and take the median of the resulting values across the entire set of hub-gene correlations. The hub-gene dscGGC effect size is based on the sampling distribution of the Fisher z-transformation $F(r)$ of a Spearman correlation coefficient r (Fieller et al., 1957), and is calculated as $(F(r_1) - F(r_2))/\sqrt{\frac{1.06}{n_1 - 3} + \frac{1.06}{n_2 - 3}}$ (where r_1 and r_2 are the sample Spearman correlation coefficients of the hub-gene pair computed using samples of size n_1 and n_2 respectively in the two conditions being compared). The bootstrap procedure involves obtaining 1000 resampled datasets within one condition (with replacement and with the same size as original data), computing the correlation coefficients in each of the resampled dataset, and comparing these correlations in each resampled dataset against the observed correlations in the same condition to derive the hub dscGGC effect size values that arises from chance alone due to sampling noise. The distribution of the resulting resampled values of the hub dscGGC effect size can then be used to compute the dscGGC hub p value as the one-sided empirical p value (given by the fraction of resampled hub dscGGC effect size values larger than the *observed* hub

dscGGC effect size when comparing the two conditions). Note that this method could yield two p values, depending on which one of the two conditions is resampled. We performed both and reported the larger of the two p values.

To increase statistical power, we choose only certain partner genes for each hub to perform the above test and consider only hubs with at least 3 such partner genes. For each gene considered as a hub in a one-sided "condition 1 vs. condition 2" (e.g., IL-10 vs. CNT) comparison, we specifically choose its partners as those genes correlated to the hub in condition 1 at FDR 40% but not in condition 2 at the same FDR cutoff. We tried FDR cutoffs of 10%, 20%, 30% and 40%, and size cutoffs (minimum number of partner genes) of 3, 4, 5 and 6, and used strength of replication of the hub dscGGC signals identified in the discovery experiment in the first validation experiment to finalize the FDR cutoff of 40% and a size cutoff of 3. The resulting set of hub dscGGC signals replicated significantly in the final unseen validation experiment for the IL-10 vs. CNT comparison alone (see Figure S3D), and seven significant dscGGC hubs were found in this IL-10 vs. CNT comparison among all tested hubs (FDR 10% in the discovery experiment followed by replication in the two validation experiments at $P < 0.1$; see Table S4, where a few dscGGC hits found in other pairwise condition comparisons besides the IL-10 vs. CNT comparison are also reported for completeness). Note that this pattern of replication of dscGGC signals occurred in the IL-10 vs. CNT comparison, but not the other comparisons, and this observation is consistent with the strong replication of scGGC signals observed separately in the IL-10 and CNT conditions (see Table S2).

To obtain the *negative control genes* discussed in the main text (as a background control for assessing the ATF2 module and extended module genes), we select all genes on the Fluidigm panel that are not part of the 30-gene ATF2 extended module and that have no correlations to ATF2 in the IL-10 condition (i.e., we exclude genes with absolute ATF2-gene correlation coefficient > 0.1 in the discovery experiment, or genes correlated to ATF2 in both validation experiments at $P < 0.2$). To serve as a better-matched background for the ATF2 extended module genes, the negative control set also focuses only on genes with detection rates of at least 50% in both IL-10 and CNT (similar to the filter used before for deriving the scGGC networks, which removes genes with low *a priori* chance of being detected as correlated in IL-10 or CNT).

Analysis of RNA-Seq Data

Tophat2 was used to map reads to perform a splicing-aware mapping (Kim et al., 2013). Mapping rate was more than 70% for all samples (see Table S6). Feature-counts tool (Liao et al., 2014) was used to quantitate the mapped reads within exons of a gene (according to UCSC hg19 gene/transcript annotations available through the Illumina iGenomes collection). DESeq2 was used for performing paired differential expression analysis of the IL-10 vs. CNT comparison (pairing is within each donor) (Table S6).

Mapping, Peak Calling and Differential Activity Analysis of the H3K27ac Sequencing Data

We sequenced H3K27ac ChIP (as well as paired genomic "input"; see above) samples from two donors in IL-10 as well as CNT conditions. Sequencing reads were mapped to the human genome (UCSC hg19 assembly) with the Bowtie2 aligner (version 2.2.2, default options) (Langmead and Salzberg, 2012). We used reference sequences, annotations and aligner indexes available through the Illumina iGenomes collection. Mapping rate was more than 90% for all samples but one (see Table S6).

H3K27ac peaks (regions of the genome enriched for H3K27ac signal) were called with HOMER (Heinz et al., 2010) using options similar to a previous study on macrophage/monocyte epigenetics (Pham et al., 2012). Specifically, for each ChIP/input sample pair, we used HOMER *findPeaks* method to find all broad peaks (1000bp (base pair) regions separated by at least 2500bp) enriched for H3K27ac signals at FDR 10%. The enrichment was derived from the number of uniquely mapped reads falling within the peak in the ChIP sample, relative to the paired input sample, using a fold enrichment cutoff of 2 and Poisson p value cutoff of 10^{-4} (note that peaks were only required to be enriched relative to the input sample, and not the local surrounding genomic background due to the "-L 0" option that we set). The approximate IP efficiency of each ChIP sample (fraction of reads mapping to peaks found in the ChIP sample) was good (at least 20%, as recommended by HOMER), and the peaks found in our CNT samples overlapped well with an independent set of previously published peaks found in untreated macrophage samples (Pham et al., 2012) (specifically, at least 62% of our CNT sample peaks overlapped with the independent peaks, and at least 79% of the peaks found in Pham et al. overlapped with our peaks). The union of peaks found across all ChIP-input sample pairs were taken and the overlapping peaks merged (using *bedtools merge* (Quinlan and Hall, 2010)) to derive a total set of 67,631 non-overlapping H3K27ac peaks, referred to as *merged H3K27ac peaks* or simply *H3K27ac peaks* in the text when the context is clear. H3K27ac is known to be an activating mark at promoters and enhancers, and our set of H3K27ac peaks could be found near genes both proximally (less than 1kb from a gene's TSS (transcription start site) in promoter region) and distally (in putative enhancer regions).

To quantitate changes in promoter/enhancer activity (i.e., H3K27c level) at the merged H3K27ac peaks between the IL-10 vs. CNT conditions, we performed a paired differential activity analysis (i.e., comparing the IL-10 vs. CNT pair for each donor) using the DESeq2 method (Love et al., 2014). Specifically, a matrix of H3K27 activities indicating the number of mapped reads (with mapping quality score at least 10) of each ChIP sample falling within each H3K27ac peak was calculated using the htseq-count tool (Anders et al., 2015), and analyzed using DESeq2 using default options and the design formula (in R's notation: "H3K7ac activity of peak ~ donor + condition").

Peaks within 1Mbp of a gene body (i.e., TSS-1Mbp to transcription end site +1Mbp) are referred to as the gene's peaks, and this operational definition is used to collect the union of peaks near a set of genes (e.g. set of ATF2 extended module genes or set of negative control genes). By using the AP1 motif enrichment analysis described next, we found that 315 of 2140 peaks near ATF2 extended module genes and 159 of 1406 peaks near negative control genes were predicted to bear AP1 binding sites (after excluding the 134 ambiguous peaks near a ATF2 extended module gene as well as a negative control gene). H3K27ac peak sequences were

scanned for enrichment of ATF2 (specifically AP1) motif using the PWMEnrich R package (Stojnic and Diez, 2015) with default options that employ a log-normal threshold-free approach to identify motif scores enrichment relative to genomic background (with log-normal distribution estimated from per-site affinity scores of a genomic background that is composed from 2kb human promoters in hg19 assembly split into 500bp regions). A p value cutoff of 0.05 was used to call H3K27ac peaks that bear AP1 motifs (and corresponded to an FDR of ~36%) – we did not correct for multiple testing here as we were more interested in the aggregate behavior of the whole set of motif-bearing peaks and not any specific motif-bearing peak. Using the output of all these analyses, we finally conduct the main test for which we used the H3K27ac data, viz., checking if there is increased enhancer activity in the IL-10 over CNT condition at AP1-motif-bearing H3K27ac peaks near ATF2 extended module genes, compared to negative control genes.

Mapping, Bidirectional Enhancer Finding, and Differential Activity Analysis of the CAGE Sequencing Data

We sequenced CAGE samples from three donors in IL-10 and CNT conditions (technical duplicate of one of the donors was done additionally). Sequencing reads were mapped with Bowtie2 as for the H3K27ac data, but with an additional step that trims the expected CAGE 3′ linker sequence inside the reads (more than 90% of all reads have the linker sequence in the expected position 28+/-1 mostly, and more rarely, at other positions, with a minimum overlap of 9 bases as computed and trimmed using the cutadapt adapter-trimming tool (Martin, 2011)). Mapping rate was more than 70% for all samples (see Table S6) and more than ~84% (11%) of the mapped reads fall within the TSS+/-1Kb sense (antisense) region respectively. These quality metrics (% of reads with CAGE linker sequence, mapping rate, and percentage within TSS) were reasonable for all samples but one (S16 CNT replicate A) and this outlying sample was discarded from further analysis.

We adopted the FANTOM5 methodology (Andersson et al., 2014; Takahashi et al., 2012) to detect bidirectionally transcribed enhancer regions (or referred simply as bidirectional enhancers) using pooled data from all samples. We detected 2866 bidirectional enhancers that were also distal from any gene exon/TSS (derived using an exon/TSS-mask file provided by FANTOM5), and promisingly 60% of these enhancers overlap with our H3K27ac peaks. We estimated the eRNA levels in these bidirectional enhancers in each sample, also using FANTOM5 tools, and then added up the eRNA levels in the two Illumina HiSeq runs in which each CAGE sample was sequenced before subjecting the resulting data available for 3 donors in IL-10 and CNT conditions to paired differential activity analysis using DESeq2, similarly as before for the H3K27ac data. Assigning enhancer regions to nearby regions and analyzing motif enrichments was also done in the same fashion as for H3K27ac peaks. At a motif enrichment p value cutoff of 0.05 (which corresponded to an FDR of ~29%), we found that 18 of 125 bidirectional enhancer regions near ATF2 extended module genes genes and 13 of 57 regions near negative control genes were predicted to bear AP1 binding sites (after excluding 3 ambiguous regions near a ATF2 extended module gene as well as a negative control gene).

A caveat with bidirectional eRNAs is that they are expressed at quite low levels in general (Andersson et al., 2014) and so they tend to suffer more from technical noise than H3K27ac data. So we performed additional sensitivity analysis of CAGE data, and found that the main test for which we used the CAGE data (i.e., ''increased enhancer activity in the IL-10 over CNT condition at AP1-motif-bearing bidirectional enhancers near ATF2 extended module genes, compared to negative control genes'') is largely robust in a ''leave-one-donor-out'' analysis. The Wilcoxon test p value of 0.04854 for this test using all three donors reported in the text changed to 0.03728, 0.1762 and 0.009854 when leaving out donor with identifier S15, S16 and S12 respectively. Note that in this leave-one-donor-out analysis, only the fold changes are updated based on the subset of patients, but the bidirectional enhancer regions were identified using FANTOM5 paper method applied on all three donors.

Selection of Putative ATF2 Binding Sites and Random Control Regions for ChIP-qPCR Validation Analysis

A pilot ATF2 ChIP-seq data generated in the IL-10 vs CNT conditions and additional criteria described below were used to manually select putative ATF2 binding sites for further qPCR validation. In detail, we had three ChIP-seq samples in the IL-10 condition of the pilot experiment and we chose the sample that yielded the most number of ChIP-seq peaks overlapping the H3K27ac peaks for further analysis. Data analysis of ChIP-seq sequencing data were the same as that for H3K27ac data, except for lowering the peak size parameter of HOMER (from 1000bp used in H3K27ac to 200bp in ChIP-seq data to find more focused regions of TF binding sites). ChIP-seq peaks selected for ChIP-qPCR validation were extended by 200bp on either side to get a 600bp sequence, which was then used for PCR primer design.

A total of 14 ChIP-seq peaks were *manually* selected for further ChIP-PCR validation guided by these criteria: i) ChIP-seq peak is co-localized within or overlapping a H3K27ac peak near any of the ATF2 extended module genes, ii) H3K7ac peaks with upregulated H3K27ac activity in IL-10 relative to CNT were preferred, iii) H3K27ac peaks that were unambiguously assignable to the nearby ATF2 extended module gene (i.e., no or few other genes in between) were preferred, and iv) H3K27ac peaks with better enrichment p value for the AP1 motif as calculated by PWMEnrich R package (Stojnic and Diez, 2015) were preferred.

A total of 4 random control regions were selected as random 600bp regions from the genome that are not within 1000bp of any ChIP-seq or H3K27ac peak.

To calculate ChIP ''percent of input'' values, the Ct values of diluted input DNA run alongside the ChIP DNA (adjusted for the dilution factor) were converted using the formula $100*2^{(\text{Adjusted Input Ct} - \text{IP sample Ct})}$. We statistically compared ATF2 binding enrichment after accounting for the effect of different donors or ChIP-qPCR regions. Specifically, for the random vs. target region comparison within each condition shown in Figure 4A, we fitted the linear model: *percent input* ~ *Donor* + *RegionType* (with *RegionType* being one of ''random'' or ''target'' regions to indicate whether the region is a random background or putative ATF2 target region, respectively) and then test if *RegionType* has a significant effect on the *percent input* to obtain the reported p values, by comparing to a model lacking

the variable of interest (*RegionType)* using R's ''anova'' function. To compare random or target regions between conditions shown in Figure 4A, we fitted the linear model: *percent input* ~ *Donor* + *Condition* + *RegionID* (with *RegionID* indicating the label of the ChIP-qPCR region; a set of 4 random (background) and 14 putative ATF2-target regions were measured) separately for random and target regions, and test for a *Condition* effect in each case. For the comparison shown in Figure 4B, the mean log percent input for the random regions for each sample was subtracted from the log percent input from the target regions to yield the log fold enrichment of the target region over the random regions. The log fold enrichment was then compared as above, using the models *log fold enrichment* ~ *Donor* + *Condition* + *TargetRegionID* (with *TargetRegionID* indicating the label of the ChIP-qPCR target region) and testing for a *Condition* effect. Having a *Donor or RegionID*/*TargetRegionID* in the above linear models allows us to have different baseline (CNT) levels for each donor or region, respectively, when computing an IL-10 vs. CNT change to mimic a paired analysis.

Analysis Involving Disease GWAS SNP Catalog, Ingenuity, and External Microarray Data

The Genome Wide Association Studies (GWAS) catalog of disease-associated SNPs was downloaded from https://www.ebi.ac.uk/gwas/ on August 2015, and restricted to SNPs associated with metabolic disease related traits (manually curated by us) where macrophage involvement has been suggested (Biswas and Mantovani, 2012). For instance, we focused on lipid traits such as cholesterol (LDL/HDL), triglycerides, and diabetes-associated traits. Those disease SNPs falling within H3K27ac peaks near the ATF2 extended module genes are reported in Table S5 (after excluding a peak that was near both an ATF2 extended module gene and a negative control gene).

To examine the expression pattern of ATF2 extended module genes in in vivo atherosclerosis plaque-associated macrophages, two separate datasets were analyzed using OMiCC (available at https://omicc.niaid.nih.gov, (Shah et al., 2016)). Data from Gene Expression Omnibus (GEO), accession number GEO: GSE7074, was used to compare gene expression in macrophages residing in atherosclerotic plaques to splenic macrophages. Data from GEO: GSE23303 was used to compare gene expression in macrophages residing in atherosclerotic plaques to plaque associated smooth muscle cells. For each study, differential expression comparisons were run in OMiCC using the default parameters. The resulting differential expression data were loaded in R and subsets of genes (the negative control set described above as well as the ATF2 module and extended module sets) were compared using t tests. For Ingenuity Pathway Analysis, the list of the ATF2 extended module genes was uploaded to Ingenuity Pathway Analysis software version 27216297 (IPA, QIAGEN Redwood City, www.qiagen.com/ingenuity), and ''Core Analysis'' was carried out with the default settings. A network was generated showing links between the ATF2 extended module genes and selected lipid metabolism pathways within the ''Diseases and Functions'' analysis output (Figure S4F).

DATA AND SOFTWARE AVAILABILITY

All sequencing and qPCR data are available in NCBI GEO under the accession number GEO: GSE81444, and the CAGE bidirectional enhancer locations, and the H3K27ac peaks/intensities available as UCSC Track Hubs (http://genome.ucsc.edu/cgi-bin/hgTracks?db=hg19&hubUrl=https://trackhub.niaid.nih.gov/upload/macseq/hub.txt).